Maximilian Weinhandl, BSc

Effect of activated carbon on the transformation pathway of amorphous calcium carbonate

Master Thesis

A thesis submitted in partial fulfilment of the requirements
for the degree of

Master of Science (MSc)

Supervisors

Univ.-Prof. Dipl.-Min. Dr.rer.nat. Dietzel Martin

Dr.rer.nat. Purgstaller Bettina, BSc MSc

Götschl Katja, BSc MSc

Institute of Applied Geosciences

Graz University of Technology

Graz, June 2021

Statutory Declaration

I declare that I have authored this thesis independently, that I have not used other than the declared sources / resources, and that I have explicitly marked all material which has been quoted either literally or by content from the used sources

02.06.2021 .....

Date

.....

Signature

Acknowledgements

Foremost, I would like to express my sincere gratitude to my supervisor Prof. Martin Dietzel and the responsible contributors Bettina Purgstaller and Katja Götschl who supported me so well during the development of this thesis and who showed so much patience in answering my endless questions. I really enjoyed and appreciated our insightful discussions, which helped me a lot in interpreting the data, and I was able to acquire a lot of new knowledge in the course of this exciting project. I would also like to express my thanks to Stefanie Eichinger and Andre Baldermann, who supported me in the analytical work and in the laboratory. Furthermore, I would also like to thank Dietmar Klammer, Dorothee Hippler, Cyrill Grengg, Andrea Wolf, Peter Schreiber, Daniela Sobian and Kelly Caroline for your great support and the great working environment. My special thanks go to my wonderful family, my dear girlfriend and my friends, who supported me endlessly throughout my studies and gave me a lot of energy in difficult times.

Abstract

Throughout the formation of crystalline $CaCO_3$ polymorphs in both biotic and abiotic environments, amorphous calcium carbonate (ACC) plays a crucial role as a precursor phase. Although numerous studies have already focused on the impact of physicochemical parameters during ACC transformation, as well as on some organic and inorganic components occurring in biogenic ACC, the controlling processes and mechanisms are still under debate. Due to the specific properties of activated carbon (AC) and the occurrence of carbon in nature with a great diversity and abundance, the influence of AC on the transformation behavior of additive-free ACC in a Mg-containing reactive aqueous solution was investigated in experiments at a pH of 8.5 ± 0.2 and temperature of 23 ± 1 °C. The results obtained showed that AC has a significant influence on the prevailing aMg^{2+}/aCa^{2+} activity ratio of the reactive solution. Furthermore, due to the narrow microporosity of AC, a partial dehydration (desolvation) of free ions occurs. Both effects have an impact on the transformation behavior of ACC. Depending on the resulting aMg^{2+}/aCa^{2+} ratios of the reactive solutions, two transformation paths resulted, where aragonite (Arg) was formed in both cases as the final polymorph: ACC transformed with the addition of 1 wt.% and 10 wt.% AC either (i) at an initial aMg^{2+}/aCa^{2+} ratio of ~6.7, first into the recently discovered metastable intermediate phase calcium carbonate hemihydrate (CCHH), or (ii) at an initial aMg^{2+}/aCa^{2+} ratio of ~8.0, first into CCHH and monohydrocalcite (Mhc) as intermediate phases, before Arg was finally formed in both cases.

The first reference experiment which was conducted without the addition of AC had the same initial chemical composition in the reactive solution as experiments performed in the presence of AC, but resulted in a direct transformation of ACC into Mg-Calcite (Mg-Cc), with a lower observed initial aMg^{2+}/aCa^{2+} ratio of ~5.5.

In the second reference experiment carried out, also conducted in the absence of AC, but with a higher initial Mg-concentration in the reactive solution, the ACC transformation pathway as well as the initial aMg^{2+}/aCa^{2+} ratio revealed strong similarities to those observed in experiments performed with the addition of AC but lower initial Mg-concentrations.

Our results suggest that AC, due to its potential to adsorb more Ca^{2+} than Mg^{2+} on its surface, significantly influences the aMg^{2+}/aCa^{2+} ratio. Thus, the presence of AC leads to increased aMg^{2+}/aCa^{2+} ratios, as well as partial dehydration of free ions and consequently to ACC transformation pathways, which can commonly be observed in reactive solutions with an increased initial Mg-concentration. In addition, in experiments with AC, we observed an increased Mg-incorporation in the solids of the final samples, where mainly Arg was detected using several analytical methods (in-situ Raman spectroscopy, ATR-FTIR, PXRD, SEM).

Kurzfassung

Bei der Bildung von kristallinen $CaCO_3$ Polymorphen, spielt das amorphe Kalziumkarbonat (ACC) als Vorläuferphase, sowohl in biotischen als auch abiotischen Milieus, eine entscheidende Rolle. Obwohl sich bereits zahlreiche Studien mit physikalisch-chemischen Parametern, sowie einigen der in biogenem ACC vorkommenden organischen und anorganischen Komponenten, welche Einfluss auf das Transformationsverhalten von ACC haben, beschäftigten, sind dennoch die Transformations-kontrollierenden Prozesse und Mechanismen immer noch schlecht verstanden. Aufgrund der spezifischen Eigenschaften von Aktivkohle (AC) und der Tatsache, dass Kohlenstoff in der Natur reichlich und mit einer großen Vielfalt auftritt, wurde der Einfluss von AC auf das Transformationsverhalten von additiv-freiem ACC in einer Mg-haltigen reaktiven Lösung bei kontrollierten pH-Bedingungen (8.5 ± 0.2), sowie Temperatur-Bedingungen (23.0 ± 1.1 °C) in diversen Experimenten untersucht. Die daraus gewonnenen Resultate zeigten, dass AC einen signifikanten Einfluss auf das in der reaktiven Lösung vorherrschende aMg^{2+}/aCa^{2+} Aktivitäts-Verhältnis hat. Weiters kommt es aufgrund der Mikroporosität von AC, zu einer teilweisen Dehydration der freien Ionen in der reaktiven Lösung. Beide Effekte haben einen signifikanten Einfluss auf das Transformationsverhalten von ACC. Abhängig von den aMg^{2+}/aCa^{2+} Verhältnissen, welche sich während der Experimente mit AC ergaben, konnten zwei unterschiedliche Transformationspfade beobachtet werden, in welchen jeweils der Aragonit (Arg) als finales Polymorph gebildet wurde: ACC transformierte bei einer Beimengung von 1 Gew.% und 10 Gew.% AC in die reaktive Lösung entweder (i) bei einem initialen aMg^{2+}/aCa^{2+} Verhältnis von ~6.7 zuerst in die kürzlich beschriebene metastabile Zwischenphase Kalziumkarbonat Hemi-Hydrat (CCHH), oder (ii) bei einem initialen aMg^{2+}/aCa^{2+} Verhältnis von ~8.0, zuerst in die beiden Zwischenphasen CCHH und Monohydrokalzit (Mhc) bevor sich final in beiden Fällen, der Arg bildete.

Das Referenzexperiment, welches ohne dem Zusatz von AC, aber derselben chemischen Zusammensetzung der reaktiven Lösung wie bei jenen Experimenten mit AC als Zusatz, durchgeführt wurde, ergab bei einem geringer initialen aMg^{2+}/aCa^{2+} Verhältnis von ~5.5 eine Transformation von ACC in Mg-Kalzit (Mg-Cc).

Das zweite, ebenfalls ohne dem Zusatz von AC, aber einer erhöhten Mg-Konzentration in der reaktiven Lösung durchgeführte Referenzexperiment, wies sowohl beim initialen aMg^{2+}/aCa^{2+} Verhältnis als auch beim Transformationspfad, starke Ähnlichkeiten zu jenen Experimenten auf, welche AC als Zusatz nutzten, jedoch eine geringe initiale Mg-Konzentration aufwiesen.

Unsere Ergebnisse vermitteln, dass aufgrund des Potentials von AC, mehr Ca^{2+} als Mg^{2+} an dessen Oberfläche zu adsorbieren, das vorherrschende aMg^{2+}/aCa^{2+} Verhältnis signifikant beeinflusst wird. Somit kommt es bei der Präsenz von AC zu erhöhten aMg^{2+}/aCa^{2+} Verhältnissen, sowie teilweisen Dehydrationen der freien Ionen und somit zu Transformationspfaden des ACC, welche üblicherweise nur bei reaktiven Lösungen mit einer erhöhten initialen Mg-Konzentration zu beobachten sind. Weiters beobachteten wir in Experimenten mit AC einen erhöhten Mg-Einbau in die Festphasen der finalen Proben, wo mittels diverser Analyseverfahren (in-situ Raman Spektroskopie, ATR-FTIR, PXRD, SEM), im Wesentlichen Arg detektiert wurde.

Abbreviations

AC	Activated carbon
ACC	Amorphous Calcium Carbonate
Arg	Aragonite
Bru	Brucite
Cc	Calcite
CCHH	Calcium Carbonate Hemihydrate
mAra	Monoclinic Aragonite
Mg-Cc	Mg-Calcite
Mhc	Monohydrocalcite
min(n)	Analyzed again (after one month)
Nes	Nesquehonite
Vat	Vaterite

Table of Content

1.Introduction

Calcium carbonate ($CaCO_3$) minerals are of great interest in the field of Earth Sciences because they play a crucial role in the global carbon cycle, as well as in ocean acidification and biomineralization and are routinely used for paleoclimatic reconstructions **(Morse and Mackenzie, 1990).** In the last decades, numerous studies have focused on the mechanisms controlling the nucleation and crystallization of biotic and abiotic $CaCO_3$ minerals **(Morse and Mackenzie, 1990; Weiner et al., 2003; Dietzel, 2011; Purgstaller et al., 2016).**

Of the well-known existing anhydrous crystalline $CaCO_3$ polymorphs occurring in marine depositional environments, calcite (Cc) and aragonite (Arg) are the most common, where Arg has a lower thermodynamic stability compared to Cc. However, vaterite (Vat) has the lowest thermodynamic stability of the three anhydrous crystalline $CaCO_3$ polymorphs. Furthermore, the hydrated thermodynamically metastable crystalline $CaCO_3$ phases monohydrocalcite (Mhc; $CaCO_3 \bullet H_2O$) and Ikaite ($CaCO_3 \bullet 6H_2O$), as well as a recently discovered third metastable hydrated crystalline phase, calcium carbonate hemihydrate (CCHH; $CaCO_3 \bullet \frac{1}{2}H_2O$) are known. **(Zou et al., 2019; Morse and Mackenzie, 1990).**

Over time, marine organisms have developed biomineralization strategies to produce $CaCO_3$ containing skeletons and functional materials such as eye lenses, protective shells (e.g. mollusks), spicules and spines (e.g. sea urchins) from the freely available Mg^{2+}, Ca^{2+} and CO_3^{2-} ions **(Politi et al., 2004; Devol et al., 2015; Aizenberg and Weiner, 2003) .** Some of them (e.g. sea urchins, foraminifera, echinoderms) are able to precisely control the incorporation of ions during the mineralization process in order to create structural elements with different compositions **(Polishchuk et al., 2017).**

Especially the sea urchin tooth is a popular example for the precise control of ion incorporation, because here, the Mg-incorporation in Cc within the same tooth can vary between 5 - 45 mol% Mg, whereby highest Mg-calcites (Mg-Cc) are located in the central part of the tooth **(Ma et al., 2009).**

It is assumed that several of these organisms are able to influence biomineralization by changing the intracellular pH at the calcification sites and thus locally controlling their aqueous solution chemistry. Nevertheless, mimicking these processes in laboratory is still challenging, since some of the mechanisms and physicochemical parameters and processes controlling this type of biomineralization are still under debate **(Xto et al., 2019).**

Numerous studies agree that the hydrated and poorly ordered amorphous calcium carbonate (ACC; $CaCO_3 \bullet nH_2O$), which occurs in various amorphous states, is an important precursor phase in the biomineralization of crystalline calcium carbonate ($CaCO_3$). Although, several of the amorphous-to-crystalline transformation mechanisms are still debated, ACC plays a key role in biomineralization strategies **(Aizenberg and Muller, 2003; Zou et al., 2019; Purgstaller et al., 2017).** In marine environments, the presence of ACC as an amorphous precursor in biomineralization has already been demonstrated in many different organisms (e.g. sea urchins larvae, crustaceans, foraminifera, ascidians, brachiopods and seabreams) **(Raz et al., 2003; Raz et al., 2002; Aizenberg and Weiner, 2003; Foran et al., 2013; Griesshaber et al., 2009; Xto et al., 2019).** It is assumed that ACC is partly responsible for large variety of $CaCO_3$ structures that can be found in nature. In addition to the fact that ACC is a metastable, highly soluble phase **(Brečević and Nielsen, 1989)**, numerous studies have already focused on the importance of magnesium, which has a significant influence on the solubility and transformation behavior of ACC, as well as on the resulting $CaCO_3$ polymorph **(Habraken et al., 2015; Blue et al., 2017; Politi et al., 2010; Loste et al., 2003, Purgstaller et al., 2019).**

Although previous studies extensively investigated the molar Mg/Ca ratios and aMg^{2+}/aCa^{2+} activity ratios of reactive solutions, as well as varying physicochemical parameters, there are still uncertainties about the reaction mechanisms controlling the transformation (e.g. solid state transformation, dissolution re-precipitation reaction) **(Radha et al., 2010; Giuffre et al., 2015; Xto et al., 2019; Konrad et al., 2016; Purgstaller et al., 2016; Gal et al., 2012)**.

This study aims to investigate the influence of activated carbon (AC) when it is present in the aqueous medium, on the metastability and the transformation behavior of synthetic additive-free ACC.

AC has specific ion adsorption / dehydration (desolvation) properties, resulting from a high porosity and a consequently large specific surface area, as well as from the chemistry and structure of the AC pore surfaces **(Marsh and Rodríguez-Reinoso, 2006; Prehal et al., 2017).** In addition, a previous study using AC with a large specific surface area, observed stronger interactions between AC and Ca^{2+} compared to AC and Mg^{2+}, in reactive solutions **(Rostamian et al., 2014).** Based on specific properties of AC and the fact that carbon occurs with great diversity and abundance in nature (e.g. organic molecules (carbohydrates, proteins), carbonates, natural gas, etc.) and can be easily transformed to elemental carbon, e.g. in coals and ashes, the influence of the additive AC on the metastable ACC was investigated in this study **(Press and Siever, 2008; Brown et al., 2011).**

For this purpose, experiments were carried out under controlled physicochemical conditions (constant T and pH), with synthesized freeze-dried ACC standard material being dispersed in reactive solutions with different solution compositions (Table 1). In several experiments, the additive AC (type: YP-80F) with very high specific surface area of 1,598 m^2/g was used, to investigate the influence of the ion adsorption behavior of AC dispersed in the aqueous solution and consequently on the mineralogical evolution of the ACC transformation.

2. Fundamentals

2.1. ACC transformation mechanisms

As soon as additive-free ACC is dispersed in the reactive aqueous solution, it partially dissolves until the solution reaches saturation with respect to ACC (SI_{ACC}) **(Konrad et al., 2018).** This triggers an ion exchange, which leads to changes in the chemical composition of both the reactive solution (e.g. alkalinity, pH, $[Ca]_{aq}$, $[Mg]_{aq}$) and the amorphous phase **(Purgstaller et al., 2019).** Among others, the free Mg^{2+} ions in the solution are partly incorporated into the ACC structure by substituting Mg^{2+} for Ca^{2+} **(Purgstaller et al., 2019),** which also contributes to an increase in $[Ca]_{aq}$. During this process, Mg-containing ACC is simultaneously formed. As already discussed by numerous studies, the transformation of the amorphous phase into a crystalline phase is triggered by a dissolution / re-precipitation reaction **(e.g. Purgstaller et al., 2017; Giuffre et al., 2015; Han and Aizenberg, 2008; Bots et al., 2012).**

Depending on composition of the reactive solution and the amorphous phase **(Purgstaller et al., 2019),** different transformation pathways have already been observed in previous studies **(Loste et al., 2003; Blue et al., 2017; Purgstaller et al., 2017)**. It has already been established that (i) the increase in the Mg-content in the ACC **(Loste et al., 2003)**, (ii) the increase in the aMg^{2+}/aCa^{2+} ratio in the reactive solution, leads to a retarded transformation and thus also significantly influences the mineralogical evolution **(Blue et al., 2016; Purgstaller et al., 2017).** While the dispersion of additive-free ACC in pure water leads to an immediate transformation into Vat and Cc, the dispersion in a reactive solution with an increased aMg^{2+}/aCa^{2+} ratio may result in a slow transformation process of the metastable Mg-ACC into the metastable Mhc **(Purgstaller et al., 2017; Konrad et al., 2018; Blue et al., 2017).** However, it is also certain that in addition to molar Mg/Ca ratios and aMg^{2+}/aCa^{2} ratios, as well as the Mg-content in ACC, other parameters (e.g. pH) also have an impact on the ACC transformation behavior **(Konrad et al., 2018)**. Although numerous studies have focused on this amorphous precursor, the parameters and mechanisms controlling the transformation are still debated **(Purgstaller et al., 2017).**

2.2. Activated carbon

Due to its excellent adsorption properties – resulting from the nanostructured porosity and consequently large specific surface area – AC is often used for the purification of water, air and the separation of gas mixtures **(Marsh and Rodríguez-Reinoso, 2006).** The different raw materials for AC production, which are mostly natural organic materials, such as wood, coconut shells and coals, as well as the different physical and chemical types of activation of AC, result in different adsorption properties of individual ACs **(Rostamian et al., 2014; Marsh and Rodríguez-Reinoso, 2006).** Although the different types of AC have different sorption behaviors (e.g. due to different pore sizes, pore proportions, surface heteroatom compounds), all ACs have a common structure, consisting of an arrangement of defective graphene layers **(Marsh and Rodríguez-Reinoso, 2006; Bansal and Goyal, 2005).**

The most important intermolecular forces are the van der Waals-forces which are mainly responsible for the molecule adsorption on AC pore surfaces **(Marsh and Rodríguez-Reinoso, 2006).** Regarding the processes that are responsible for removal of ions from an aqueous solution, there are several suggestions (e.g. ion exchange due to surface complexation, narrowness of pores or the HSAB (hard and soft acids and bases) concepted by **Alfarra et al. (2004)**) **(Marsh and Rodríguez-Reinoso, 2006).**

Furthermore, AC has the ability to partially dehydrate (desolvate) dissolved ions. This property is reinforced by the decrease in pore sizes **(Prehal et al., 2017)**.

2.3. Transition phase CCHH

Calcium Carbonate Hemihydrate (CCHH; $CaCO_3 \bullet ½H_2O$) was first discovered and described by **Zou et al. (2019)**. It was found that compared to the Mhc, CCHH only incorporates half the amount of water into its structure. In the study of **Zou et al. (2019)**, a monoclinic structure was suggested for pure CCHH, which, however, has already been refuted in the recent study of **Aufort and Demichelis (2020)**. They suggested that pure CCHH has an orthorhombic structure and that a monoclinic structure only results when Mg^{2+} is incorporated into its structure, as this leads to a distortion of the unit cell. Since Mg^{2+} typically occurs sixfold coordinated and eightfold coordinated with oxygen ions **(Németh et al., 2018)** and Ca^{2+} occurs eightfold coordinated in CCHH, Mg^{2+} can be substituted for Ca^{2+}, which enables Mg-incorporation into the structure of CCHH.

Note here, that CCHH could not be detected in earlier studies. Since some regions of the Raman spectra as well as FTIR spectra but also the needle-shaped morphology of CCHH and Nes show strong similarities (Table 2), the CCHH may have been incorrectly interpreted as Nes in some former studies. For example, **Konrad et al. (2018)** detected the presence of Nes in some of their experiments just by using in-situ Raman spectroscopy analysis and FTIR spectroscopy analysis. Nevertheless, Nes could only be detected once by using SEM **(Konrad et al., 2018).** Since CCHH is a thermodynamically metastable phase, it could have already transformed before SEM analysis. On the other hand, the needle-shaped morphology on the SEM images may had been incorrectly described as Nes.

3.Methods

3.1. Synthesis of ACC

For the synthesis of ACC standard material, a 1 M calcium chloride ($CaCl_2$) solution and a 1 M sodium carbonate (Na_2CO_3) solution were prepared by mixing calcium chloride dihydrate ($CaCl_2 \bullet 2H_2O$) and sodium carbonate (Na_2CO_3) chemicals with ultrapure water (Milli-Q water; 18.2 MΩ cm). These two solutions provided the Ca^{2+} and CO_3^{2-} sources for the synthesis of ACC. The two stock solutions were diluted with ultrapure water to obtain a concentration of 0.25 M, each with a volume of 80 ml. The two solutions were quickly mixed in a beaker (pH ~10, T = 10 ± 1 °C and transferred to a suction filtration unit in order to separate the reaction products from the solution using a membrane cellulose acetate filter (0.2 µm pore size; 10 cm diameter). In order to remove the NaCl from the separated reaction products, it was washed with pre-cooled (5 ± 1 °C) ultrapure water (Milli-Q water). The NaCl-free reaction products were then dried using the BenchTop pro™ freeze dryer (-50 °C condenser temperature), to remove the non-structure-bound H_2O (Fig. 1) **(Konrad et al., 2016).** The freeze-dried ACC-powder was then stored airtight in a desiccator with silica gel (relative humidity = 3%; 22 ± 2 °C) in order to maintain its condition and to avoid transformation **(Konrad et al.; 2018).**

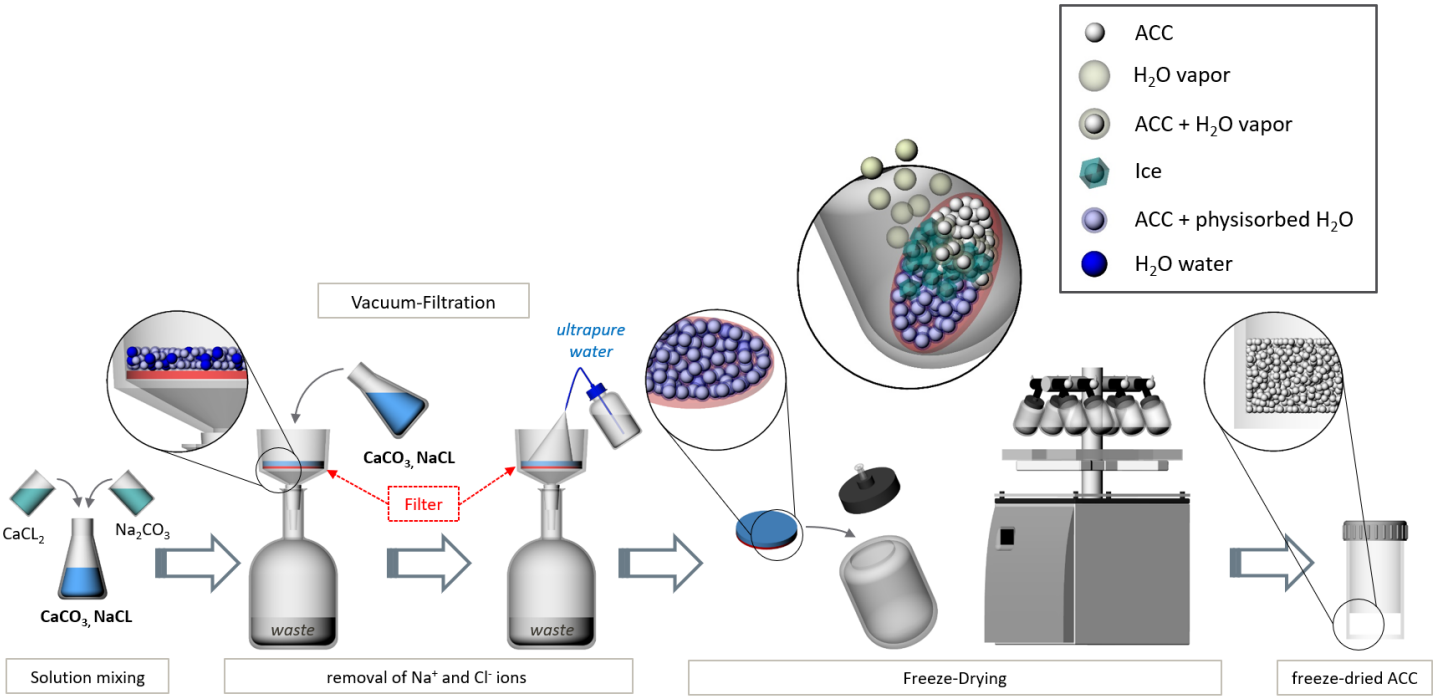

*Fig. 1: Experimental setup for the synthesis of ACC (adapted from **Konrad et al., 2016**).*

3.2. Experimental setup for ACC transformation into crystalline Ca-Mg carbonates

Transformation experiments of ACC into crystalline Ca-Mg carbonates were performed using an experimental setup adapted from **Konrad et al. (2018).** The experimental setup consists of a stirring plate equipped with a 250 ml borosilicate glass reactor (23 ± 1 °C), an in-situ Raman spectroscope (Raman RXN1™ from Kaiser opitcal systems™) and a titrating unit (SI Analytics Titrator TitroLine™) (Fig. 2). The experiments were carried out in a temperature-controlled room at 23 ± 1 °C. For the experiments, 50 ml of $MgCl_2$ - $NaHCO_3$ solutions were prepared by mixing $NaHCO_3$ and $MgCl_2 \bullet 6H_2O$ chemicals with ultrapure water. The $NaHCO_3$ concentration is identical in all experiments (100 mM), while the $MgCl_2$ concentration is either 50 mM (exp. Mg50) or 30 mM (exp. Mg30, 30_AC1, 30_AC10a, 30_AC10b, 30_AC1; see Table 1). In experiments 30_AC1, 30_AC10a and 30_AC10b certain amounts of AC were added into the $MgCl_2$ - $NaHCO_3$ solutions (Table 1) which was stirred at 200 rpm.

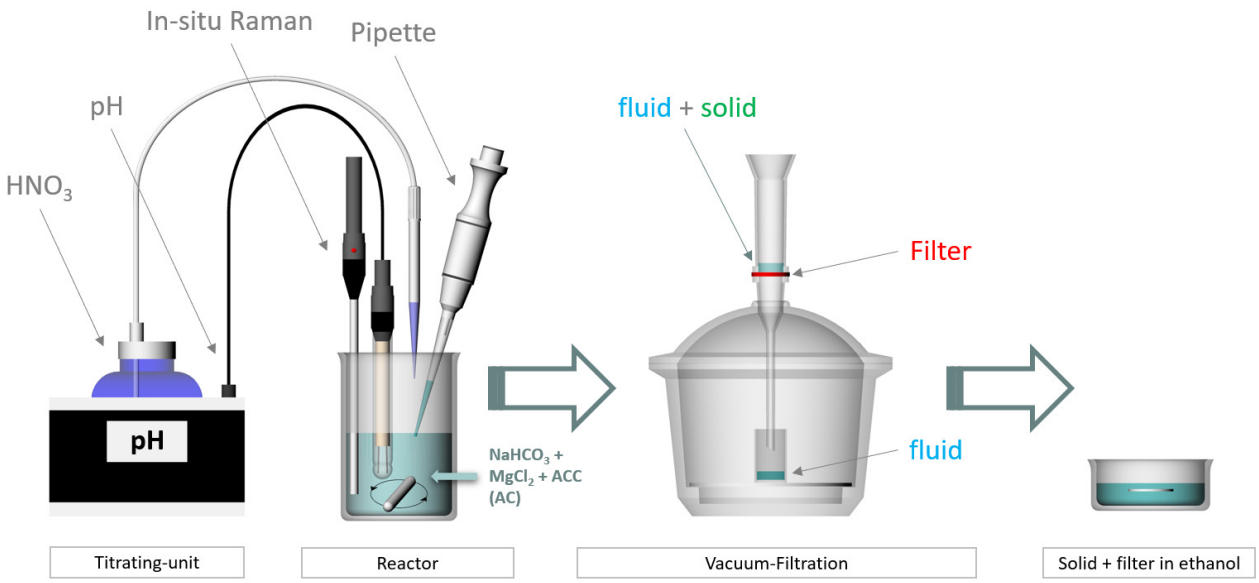

Fig. 2: Experimental setup for ACC transformation into crystalline Ca-Mg carbonates.

Subsequently, a pre-weighed amount of synthesized ACC (1.5 g) was dispersed in the stirred glass reactor filled with the $MgCl_2$ - $NaHCO_3$ - (AC) solution. In order to keep the pH (8.5 ± 0.2) stable during the experimental run, the titrating unit (SI Analytics Titrator TitroLine™) automatically added 0.5 M NaOH solution at addition steps of 0.1 ml. The pH was measured with a Schott Blueline probe, which was calibrated against NIST buffer standard solutions at pH 4.01, 7.00 and 10.00.

The mineralogical evolution of the precipitates was monitored using in-situ Raman Spectroscopy Raman RXN1™ (Kaiser optical systems™) with a Kaiser MR Probe head equipped with a quarter-inch immersion optic (wavelength = 785 nm). The spectra were recorded in a range of 100 - 3424 cm^{-1} and a resolution of 1 cm^{-1} with an exposure time of 60 sec for a period of up to 24 hours. The Raman spectra of the samples collected after one week of reaction time were recorded for a period of 10 min. The baseline of the individual Raman spectra was corrected using the Pearson´s method in the iC Raman™ 4.1 software (Kaiser optical system™).

In each of the experiments, homogeneous sub-samples of the reactive suspension were taken using a pipette (2 ml) at defined time steps (about 10 min, 20 min, 60 min) and when visible changes in the in-situ Raman spectrum occurred (Table 3). The solids were separated from the remaining solution using a 0.2 µm membrane cellulose acetate filter and a suction filtration unit, then rinsed with ethanol and then dried in an oven at 40 °C in order to use them for further ex-situ analysis. Immediately after filtration, 0.1 g of the solution was used for the measurement of the total alkalinity (TitroLine alpha plus titrator; Schott instruments™). The analytical precision of the alkalinity measurement is ± 2%. Furthermore, 0.5 g of the remaining solution was diluted with 2% HNO_3 for chemical analysis.

Table 1: Initial composition of the experimental solutions for ACC transformation used in the study.

experiment	*pH*	*$NaHCO_3$ [mM]*	*$MgCl_2$ [mM]*	*AC [wt.%]*
Mg50	8.4	100	50	-
Mg30	8.4	100	30	-
30_AC1	8.5	100	30	1
30_AC10a	8.5	100	30	10
30_AC10b	8.4	100	30	10

3.3. Analytical procedures

After the separated solids of the sub-samples were dried, their mineralogical compositions were determined using Fourier transform infrared spectroscopy (FTIR) in attenuated total reflectance (ATR) mode. The examination area was 650 - 4000 cm^{-1}, with a resolution of 4 cm^{-1}. The mineral phases of the solids were then analyzed in the 2Θ range of 4 - 85° using powder X-ray diffraction (PXRD) (PANalytical X´Pert PRO diffractometer) with Co-Kα-radiation and solid-state real time multiple strips. The parameters during the measurements were 40 mA, 40 kV, 0.008°/step and 40 s/step. The mineral phases were evaluated using the PANalytical X´Pert HighScore Plus software with the PDF-2 database. A scanning electron microscope (SEM; ZEISS DSM 982 Gemini) equipped with a field emission electron gun operating at 5 kV was used to display selected precipitates (gold-coated)**.**

For the determination of the elementary compositions, the solids of the sub-samples were digested in 6% suprapure HNO_3. The solutions of the sub-samples and digested solids were examined by inductively coupled plasma optical emission spectroscopy (ICP-OES; Perkin Elmer Optima 8300 DV) with an analytical error for Ca und Mg < ± 3%.

To determine the Mg-contents ($[Mg]_{solid}$; mol% Mg; Table 4) of the solids, contents were measured either directly after digestions with 6% HNO_3 by ICP-OES, or were estimated by mass balance calculations of the reactive solution sampled at certain time steps according to the equation

$$[Mg]_{solid} = \frac{{}^{n}Mg}{{}^{n}Mg + {}^{n}Ca} \times 100 \qquad (Eq. 1)$$

where ${}^{n}Mg$ and ${}^{n}Ca$, which were calculated from the chemical data of the solution by subtracting the measured Mg- and Ca-concentrations from the completely available concentrations, correspond to the moles of Mg^{2+} and Ca^{2+} in the solid phase. Note here that the mass balance calculation does not consider the influence by AC (e.g. by adsorption) and the results are therefore only approximations to the true values and are used for comparison.

While the total available Mg-concentrations were derived by their initial concentrations (before ACC was dispersed), the total available Ca-concentrations were derived from the 1.5 g ACC ($CaCO_3 \bullet 0.4H_2O$; 107.3 g/mol; **Konrad et al.; 2016).** Note here that the Mg-contents of the crystalline bulk solids estimated by both approaches – direct measurement and mass balance calculations – are in reasonable agreement, whereas the estimated Mg-contents of solid samples that contain amorphous phases exhibit higher values when directly measured.

3.4. Hydrochemical modeling

The PHREEQC software was used to calculate the aqueous speciation, saturation degrees and ion activities of the reactive solutions (Table 5). For the calculations, the edited database *MINTEQ.V4* was used **(Nes: Wang and Li (2012); ACC: Brečević and Nielsen (1989); Mhc: Kralj and Brečević (1995)).**

4.Results

4.1. Solid phase characterization

4.1.1. Experiments without AC

In total, two ACC transformation experiments were conducted without AC as an additive (exp. Mg50, Mg30). The initial Mg-concentration of the solution is 50 mM in exp. Mg50 and 30 mM in exp. Mg30 (Table1).

The in-situ Raman spectra, which enable a qualitative monitoring of aqueous carbonate species, showed within the first 5 min in all experiments an aqueous HCO_3^- band at ~1018 cm^{-1} (C-OH stretch) and ~1363 cm^{-1} (symmetric stretch), as well as a single aqueous CO_3^{2-} band at ~1067 cm^{-1} **(Purgstaller et al., 2016; Geisler et al., 2012).** The initial intensity of the HCO_3^- band is, however, higher than the band of the dissolved CO_3^{2-}, owing to the predominance of HCO_3^- aqueous species at the working pH 8.5 ± 0.2 **(Purgstaller et al., 2016).** After adding the ACC into the initial solutions, the characteristic v_1 Raman band of ACC became visible in the in-situ Raman spectrum at ~1081 cm^{-1} and was present for distinct periods of time (Table 3)**.**

As ACC transformed into crystalline carbonate phases, the v_1 band of ACC decreased and characteristic bands of distinct crystalline carbonate phases evolved **(Purgstaller et al.; 2016)**. During this time, CO_3^{2-} ions are removed from the solution as indicated by the decrease of the aqueous HCO_3^- and CO_3^{2-} Raman bands**.**

In the case of experiment Mg50, the collected in-situ Raman spectra indicated the transformation of ACC into CCHH in the solution after ~50 min of reaction time (Fig. 3).

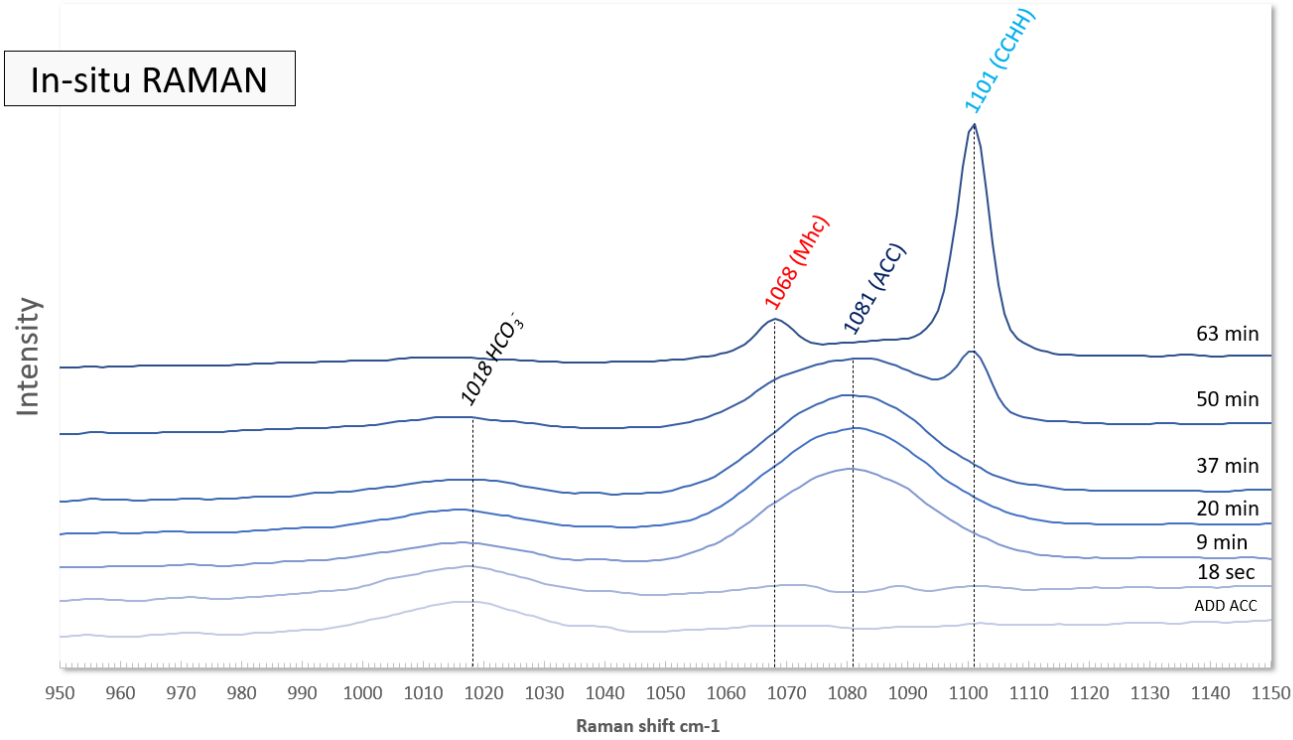

Fig. 3: In-situ Raman spectra from Mg50 showing the temporal evolution of ACC transformation into Mhc and CCHH.

CCHH has a strong v_1 band at ~1101 cm^{-1} (Fig. 3) and a weak v_4 band at ~700 cm^{-1} (not shown), which agrees with the Raman measurement data from the previously published work on CCHH **(Zou et al, 2019).** From the reaction time of ~63 min, Mhc was also visible in the spectrum, characterized by a strong v_1 band at ~1068 cm^{-1} (Fig. 3) and a weak v_4 band at ~699 cm^{-1} (not shown). These data also agreed with those from the published literature **(Purgstaller et al., 2017).**

X-ray diffraction (XRD) results of the dried precipitates of experiment Mg50 from 50 min onwards confirmed the presence of traces of Mhc and showed unidentified peaks at Bragg spacings (*d*) of 5.31 Å, 5.22 Å, 3.03 Å, 2.50 Å (Fig. 4). The latter values are in excellent agreement with those reported for CCHH in the study of **Zou et al. (2019).**

The sample, which was collected after 63 min of reaction time, was analyzed again after one month using XRD. It was found that CCHH and Mhc was completely transformed into Arg and Cc after this period (labeled as 63 min (n) in Fig. 4).

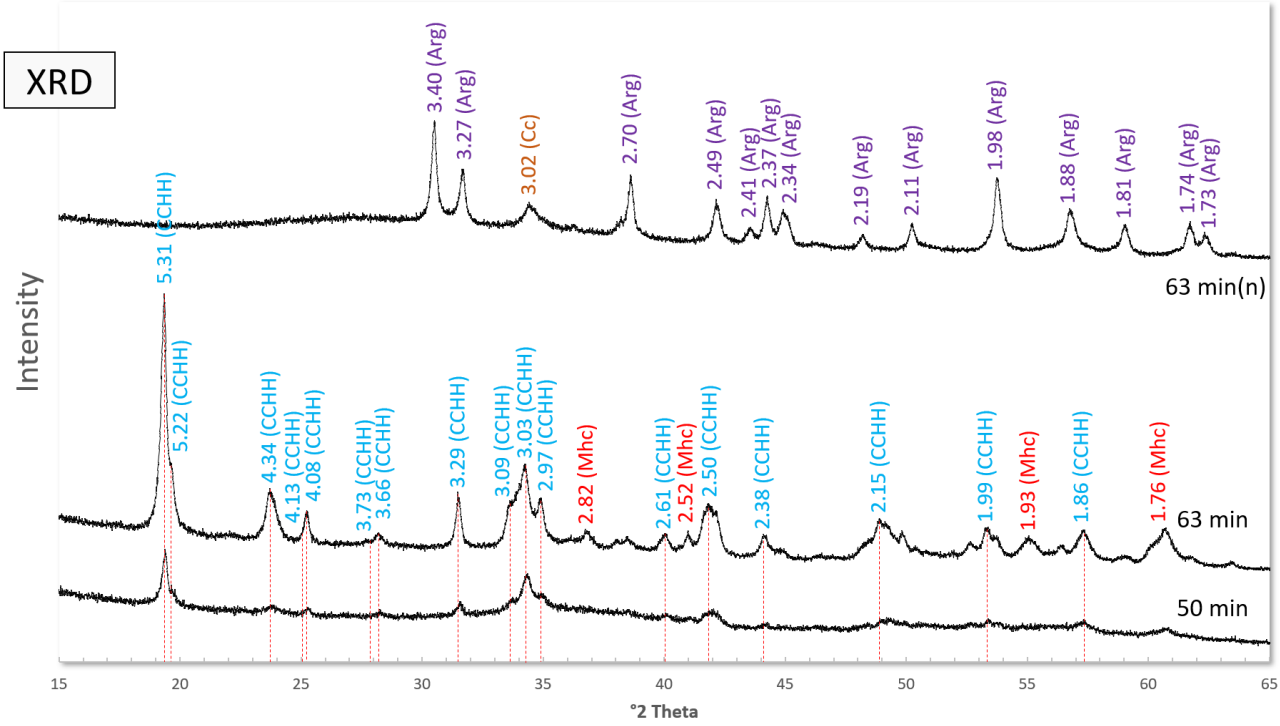

*Fig. 4: The main characteristic CCHH peaks of Mg50 (blue values) after 50 min and 63 min of reaction time, compared to the main CCHH peaks identified by **Zou et al. (2019)** (dashed lines in red), which match perfectly. Values in red show characteristic Mhc peaks (Ref. Code: 98-004-5764). Values in purple (63 min(n)) show characteristic Arg peaks (Ref. Code: 98-000-5272) and values in brown (63 min(n)) show characteristic Cc peaks (Ref. Code: 98-000-5340).*

The scanning electron microscope (SEM) images of the precipitates of Mg50, sampled after ~50 min of reaction time, showed aggregates (~1 - 2 µm) of platelet-shaped CCHH-crystals (Fig. 5A - B), as well as larger amounts of spheroidal-shaped ACC-particles in a size range of 50 - 200 nm and an average size of ~100 nm (Fig. 5B) **(Konrad et al., 2016).**

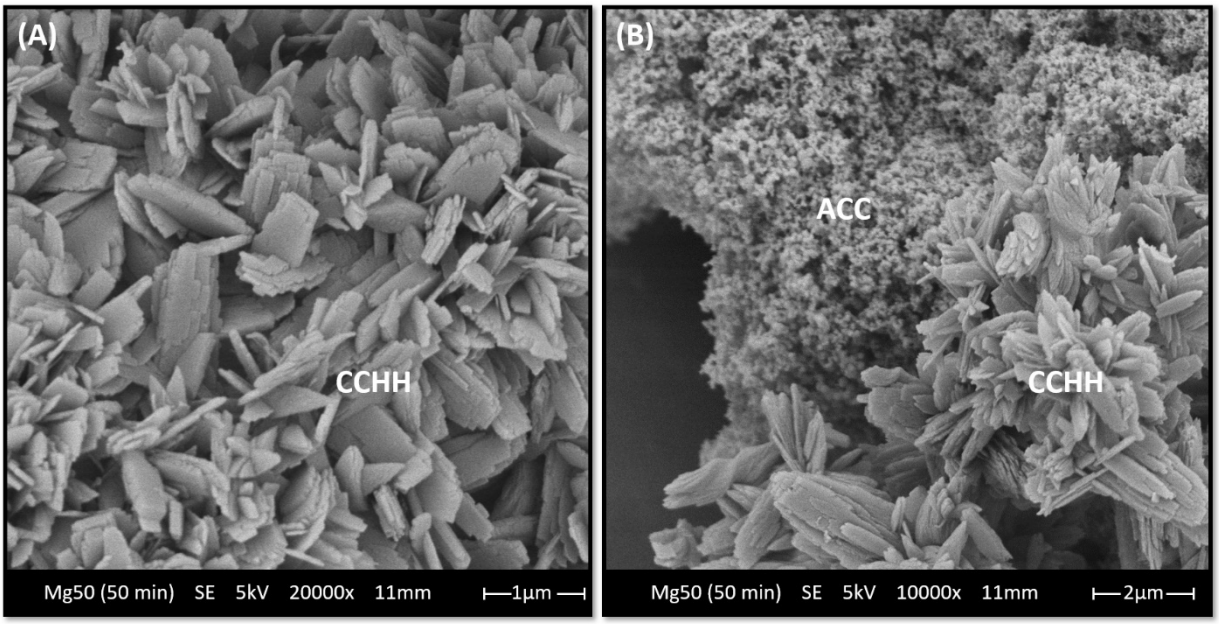

Fig. 5: SEM images of dried precipitates with different magnifications. ACC and CCHH-crystals formed in Mg50 after ~50 min of reaction time.

Note here that the presence of CCHH in the collected solids could not be confirmed by ATR-FTIR analysis in this experiment, because of alteration of the CCHH to Cc and Arg during the storage of the sample (Table 1).

In the case of the second experiment (Mg30), with the lower Mg-concentration (30 mM) the transformation of the ACC took place at an earlier point in time than in Mg50. A strong v_1 band at ~1088 cm^{-1}, a v_4 band at ~714 cm^{-1} and a vibration mode of ~284 cm^{-1} from a reaction period of at least 21 min indicated the formation of Mg-Cc ($Ca_xMg_{x-1}CO_3$) via ACC in the collected in-situ Raman spectra **(Bischoff et al., 1985).** Mg-Cc remained stable until the end of the experiment (Fig. 6).

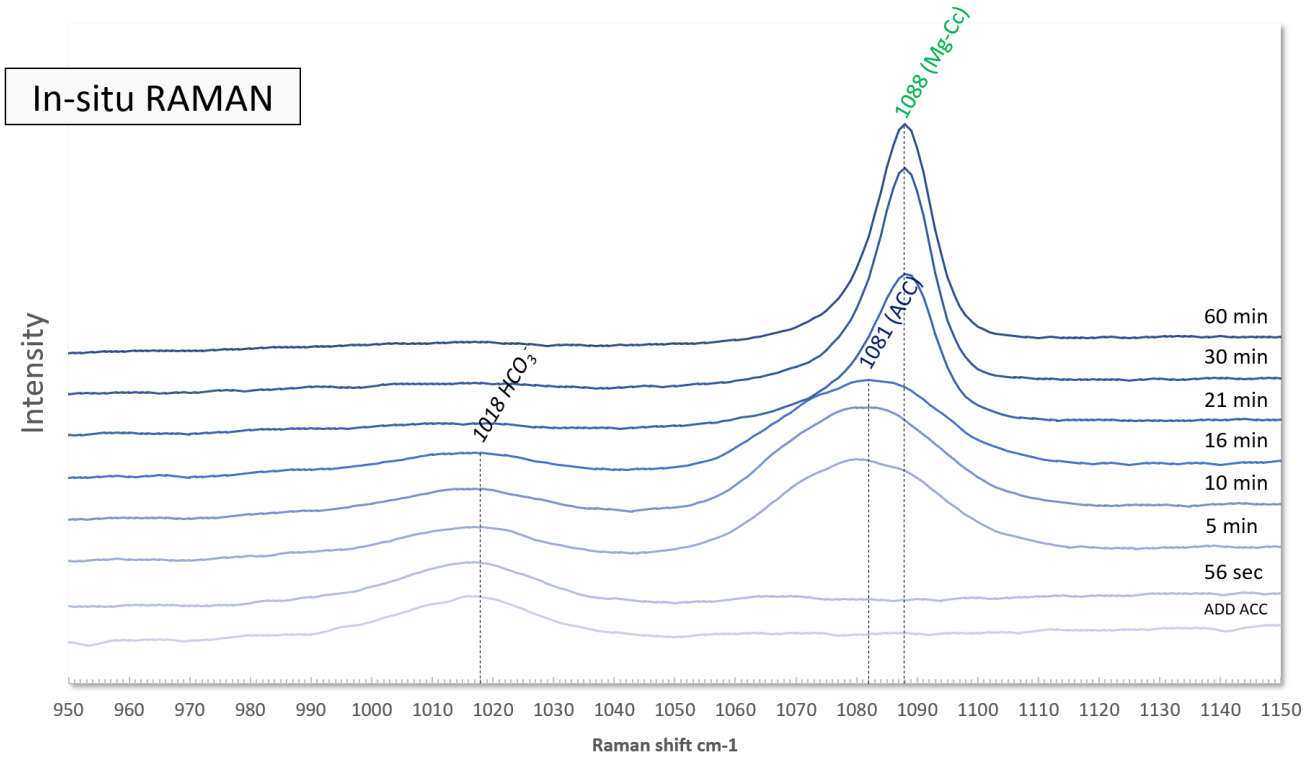

Fig. 6: In-situ Raman spectra of Mg30 showing the temporal evolution of ACC transformation into Mg-Cc.

XRD results confirmed the presence of Mg-Cc in the reaction product sampled after 60 min of the reaction time (Fig. 7).

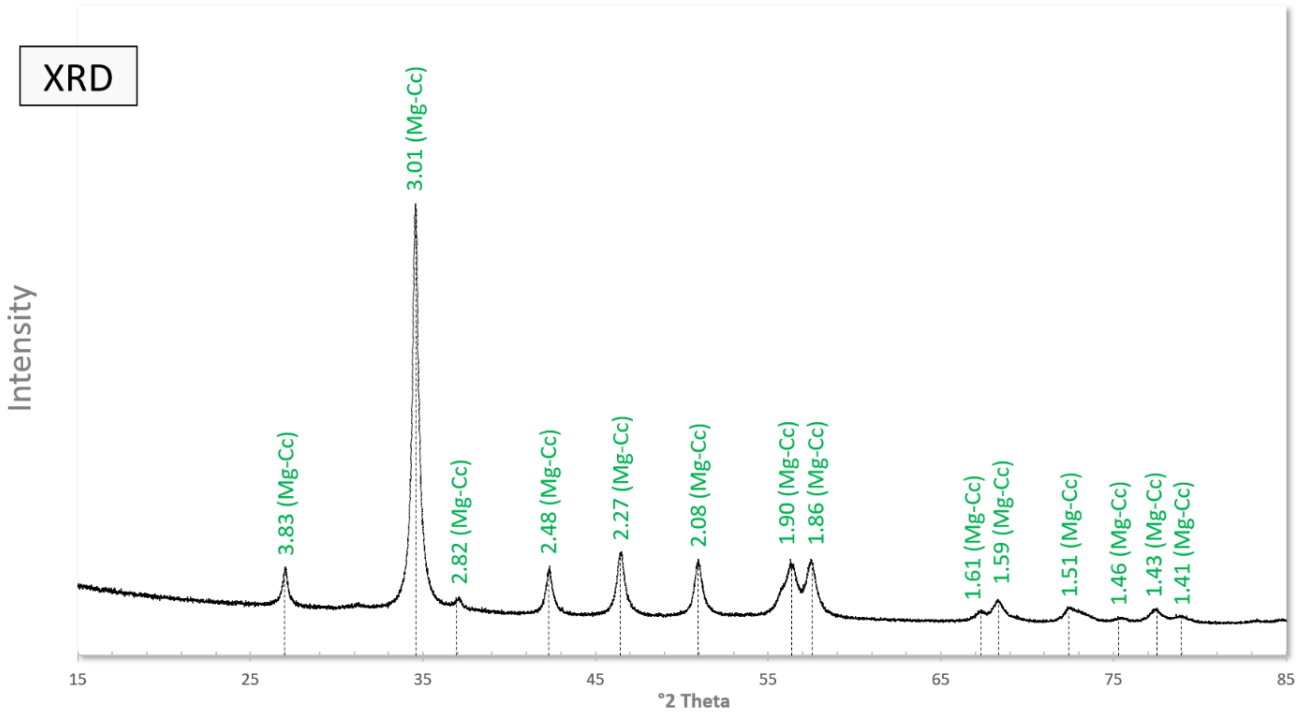

Fig. 7: XRD Mg-Cc Peaks of Mg30 (60 min) (Ref. Code: 98-004-1829).

The presence of Mg-Cc in the samples was also shown by ATR-FTIR spectra. The Mg-Cc bands v_1 at ~1086 cm^{-1}, v_2 at ~848 cm^{-1} and v_4 at ~715 cm^{-1} (Table 1) agree with those bands from **Purgstaller et al. (2017).** SEM images of the sample collected after 60 min showed aggregates (~300 - 500 nm) of rhombohedral Mg-Cc-crystals (Fig. 8).

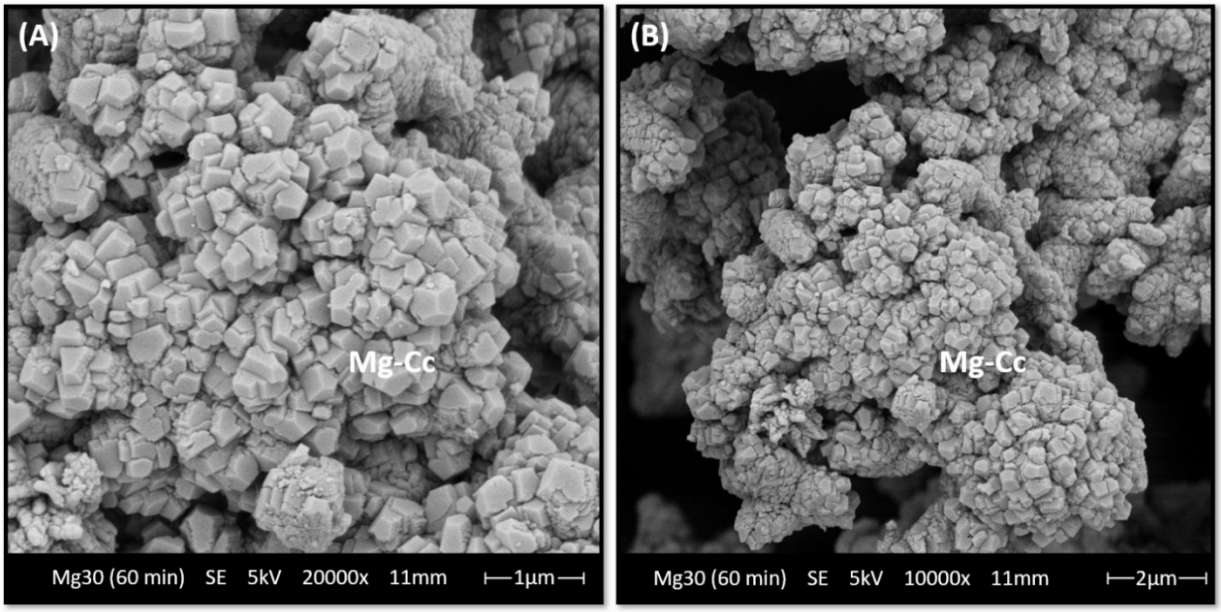

Fig. 8: SEM images of dried precipitates with different magnifications. Mg-Cc-crystals formed in Mg30 after 60 min of reaction time.

Table 2: Characteristic Raman shifts (cm^{-1}) and ATR-FTIR spectroscopic data (cm^{-1}) of the obtained carbonate phases

Carbonate Phase	Study	Raman			Study	ATR-FTIR		
		v_1	v_4	*Libration mode*		v_1	v_2	v_4
ACC	***Wang et al. (2012)***	1080	--	--	***Loste et al. (2003)***	1072	863	--
Monohydrocalcite	***Coleyshaw et al. (2003)***	1069	723 / 699	208	***Coleyshaw et al. (2003)***	1063	872	762 / 698
CCHH	***Zou et al. (2019)***	1102	700	--	***Zou et al. (2019)***	1096	860	692
Nesquehonite	***Coleyshaw et al. (2003)***	1100	705	--	***Coleyshaw et al. (2003)***	1099	854	719
Calcite	***Edwards et al. (2005)***	1086	713	283	***Böttcher et al. (1997)***	1084	876 / 848	712
Mg-Calcite	***Bischoff et al. (1985)***	1087	714	284	***Böttcher et al. (1997)***	1086	875 / 848	715
Aragonite	***Kontoyannis et al. (2000)***	1084	705 / 700	205 / 152	***Andersen et Brečević (1991)***	1083	854	713 / 700

Table 3: Mineralogical composition of the precipitates, obtained by in-situ Raman *(cm^{-1})*, XRD and ATR-FTIR *(cm^{-1})* analysis.

Experiment	**time**	**Raman**			**Mineralogy**	**ATR - FTIR**				**Mineralogy**	**XRD**
	sec/min/h/week	v_1	v_4	Libration mode		v_3	v_1	v_2	v_4		Mineralogy
Mg50	18 sec	--	--	--	--	--	--	--	--	--	--
24.2 ± 0.7 °C	9 min	1081	--	--	ACC	--	--	--	--	--	--
--	20 min	1081	--	--	ACC	--	--	--	--	--	--
	37 min	1081	--	--	ACC	--	--	--	--	--	--
	50 min	1081 / 1101	--	--	ACC / CCHH	--	--	--	--	--	ACC / CCHH
	63 min	1068 / 1101	700	--	Mhc / CCHH	--	--	--	--	--	Mhc / CCHH
	63 min(n)	--	--	--	--	--	1083	854	713 / 700	Arg	Arg / Cc
Mg30	0 sec	--	--	--	--	--	--	--	--	--	--
23.9 ± 1.2 °C	56 sec	--	--	--	--	--	--	--	--	--	--
--	5 min	1081	--	--	ACC	--	--	--	--	--	--
	10 min	1081	--	--	ACC	--	--	--	--	--	--
	16 min	1081	--	--	ACC	--	--	--	--	--	--
	21 min	1088	714	284	Mg-Cc	--	1086	848	715	Mg-Cc	Mg-Cc
	30 min	1088	714	284	Mg-Cc	--	1086	848	715	Mg-Cc	Mg-Cc
	60 min	1088	714	284	Mg-Cc	--	1086	848	715	Mg-Cc	Mg-Cc
30_AC1	0 sec	--	--	--	--	--	--	--	--	--	--
22.0 ± 0.8 °C	22 sec	--	--	--	--	--	--	--	--	--	
1 wt.% AC	6 min	1082	--	--	ACC	--	--	--	--	--	--
	11 min	1082	--	--	ACC	--	--	--	--	--	--
	21 min	1082	--	--	ACC	--	--	--	--	--	--
	30 min	1082 / 1101	--	--	ACC / CCHH	--	--	--	--	--	--
	61 min	1085 / 1101	705	205	Arg / CCHH	--	--	--	--	--	Arg / CCHH
	24 h	1085	705	205 / 152	Arg	--	1083	854	713 / 700	Arg	Arg
	1 week	1085	705	205 / 152	Arg	--	1083	854	713 / 700	Arg	Arg
	61 min(n)	--	--	--	--	--	1083	854	713 / 700	Arg	Arg / Cc

Table 3: Mineralogical composition of the precipitates, obtained by in-situ Raman *(cm^{-1})*, XRD and ATR-FTIR *(cm^{-1})* analysis.

Experiment	**time**	**Raman**			**Mineralogy**	**ATR - FTIR**				**Mineralogy**	**XRD**
	sec/min/h/week	v_1	v_4	Libration mode		v_3	v_1	v_2	v_4		Mineralogy
30_AC10a	0 sec	--	--	--	--	--	--	--	--	--	--
22.0 ± 0.9 °C	31 sec	--	--	--	--	--	--	--	--	--	--
10 wt.% AC	5 min	1082	--	--	ACC	--	--	--	--	--	--
	10 min	1082	--	--	ACC	--	--	--	--	--	--
	16 min	1082	--	--	ACC	--	--	--	--	--	--
	22 min	1082	--	--	ACC	--	--	--	--	--	--
	31 min	1101	--	--	CCHH	--	1072 / 1096	860	692	ACC / CCHH	ACC / CCHH
	59 min	1101	700	--	CCHH	--	1096	860	692	CCHH	CCHH
	1 week	1085	705	205	Arg	--	1083	854	713 / 700	Arg	Arg
30_AC10b	0 sec	--	--	--	--	--	--	--	--	--	--
23.1 ± 0.8 °C	5 min	1082	--	--	ACC	--	--	--	--	--	--
10 wt.% AC	10 min	1082	--	--	ACC	--	--	--	--	--	--
	20 min	1082	--	--	ACC	--	--	--	--	--	--
	40 min	1082	--	--	ACC	--	--	--	--	--	--
	60 min	1101	700	--	CCHH	--	1096	860	692	CCHH	CCHH
	70 min	1101	700	--	CCHH	--	1096	860	692	CCHH	CCHH
	99 min	1101	700	--	CCHH	--	1096	860	692	CCHH	CCHH
	102 min	1101	--	--	CCHH	--	1096	860	692	CCHH	CCHH
	24 h	1068 / 1085	700	152	Mhc / Arg	--	1063	872	762 / 698	Mhc	Mhc
	1 week	1068 / 1085	705	152	Mhc / Arg	--	1083	872 / 854	762 / 713 / 700	Mhc / Arg	Mhc / Arg / Nes

4.1.2. Experiments with AC

In total, three experiments were carried out with the addition of AC (30_AC1, 30_AC10a, 30_AC10b). The initial Mg-concentration of those experiments was identical to that of experiment Mg30 which was performed without AC (Table 1). As for the experiments without AC, an aqueous HCO_3^- band at ~1017 cm^{-1} (C-OH stretch) and ~1363 cm^{-1} (symmetric stretch), and a single aqueous CO_3^{2-} band at ~1067 cm^{-1} in the in-situ Raman spectra were also visible here **(Purgstaller et al., 2016).** However, both the HCO_3^- bands and the v_1 bands of ACC (~1082 cm^{-1}) in the experiments with AC showed lower initial intensities than in the experiments without AC.

In experiment 30_AC1 (1 wt.% AC) the transformation of the ACC into CCHH occurred at ~30 min. The formation of the crystalline phase CCHH is recognizable by the rise of Raman bands v_1 at 1101 cm^{-1} (Fig. 9) and v_4 at 700 cm^{-1}. From a reaction time of at least 61 min, in addition to the characteristic CCHH bands, the bands v_1 at 1085 cm^{-1}, v_4 at 705 cm^{-1} and libration mode at 205 cm^{-1} corresponding to Arg are observed. At 24 hours, characteristic CCHH bands can no longer be found in the in-situ Raman spectra and only Arg is detected in the reactive solution, which remains stable until the end of the experiment after one week (Fig. 9).

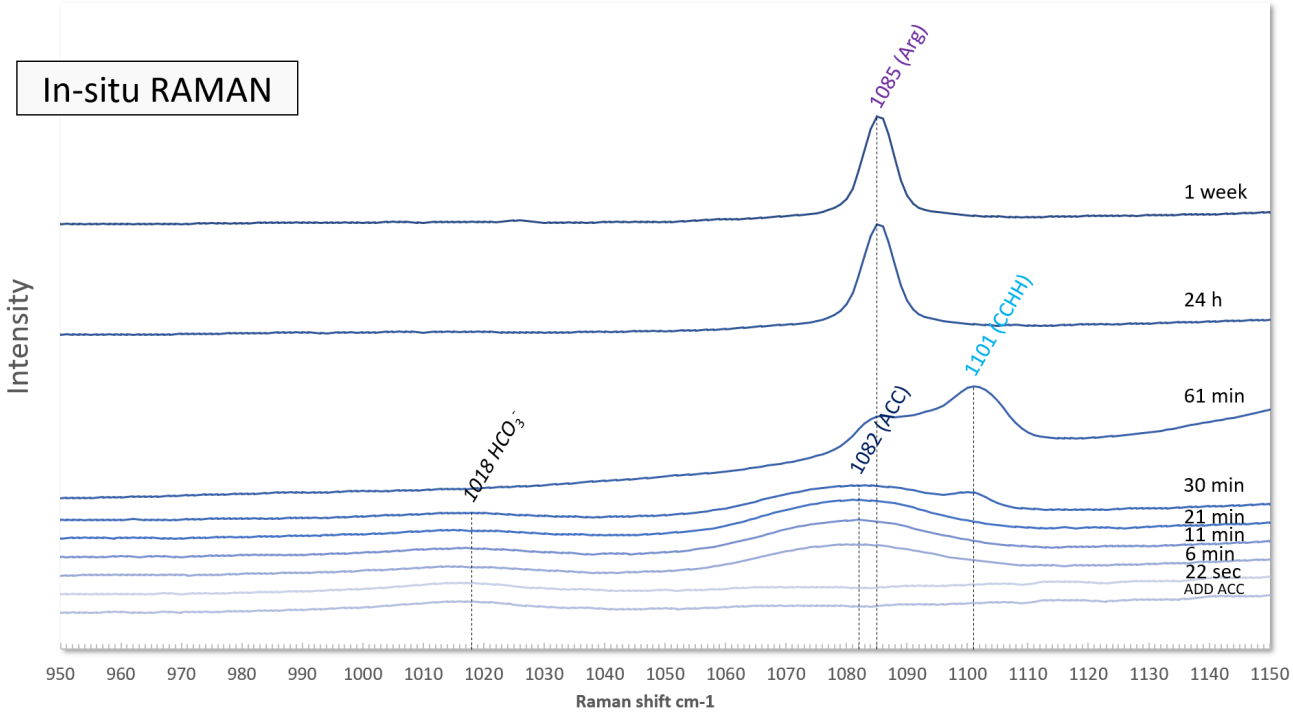

Fig. 9: In-situ Raman spectra of 30_AC1 showing the temporal evolution of mineral precipitation.

Characteristic CCHH peaks can only be found in the XRD pattern after ~61 min of reaction time (Fig. 10). Samples which were collected between 24 h and one week showed only Arg (Table 3).

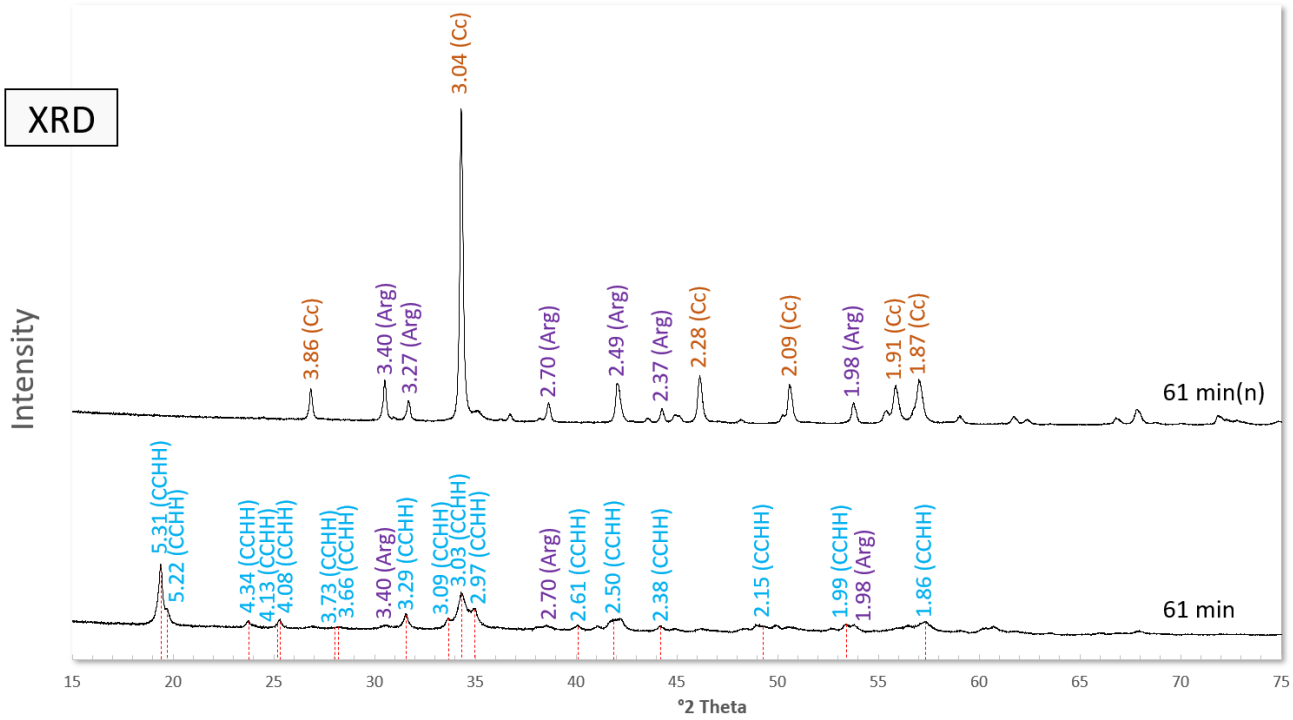

*Fig. 10: The dashed red lines indicate the XRD CCHH peaks identified by **Zou et al. (2019)** compared to the CCHH peaks (61 min) and Arg peaks (purple values; Ref. Code: 98-000-5272) and Cc peaks (brown values; Ref. Code: 98-002-1939) (61 min(n)) of 30_AC1.*

Note here that the presence of CCHH in the collected solids could not be confirmed by ATR-FTIR analysis in this experiment, because analytical errors occurred within a reaction time of 0 - 61 min (Table 3). The ATR-FTIR spectra of samples collected at later times (> 61 min) showed only Arg, recognizable by the characteristic bands v_1 at ~1083 cm^{-1}, v_2 at ~854 cm^{-1} and v_4 at ~700 cm^{-1} and ~713 cm^{-1}.

The sample which was collected after the reaction time of ~61 min, was analyzed again after one month (labeled 61 min(n)) using ATR-FTIR and XRD. It was found that CCHH was completely transformed or altered into Cc and Arg after one month (61 min(n) in Fig. 10; Table 3) when the solid sample was stored under dry conditions in a desiccator.

SEM images of the altered precipitates (61 min(n); Fig. 11 A - B) show predominately ~200 - 1500 nm rhombohedral Cc-crystals with rounded corners forming elongated aggregates. Images of the precipitates of 30_AC1 collected after one week of reaction time, showed Arg that form ~100 - 300 nm crystals aggregating into ~2 - 5 µm sized rods (Fig. 11 C - D). Due to the small amount of AC in 30_AC1, AC particles could not be detected by SEM.

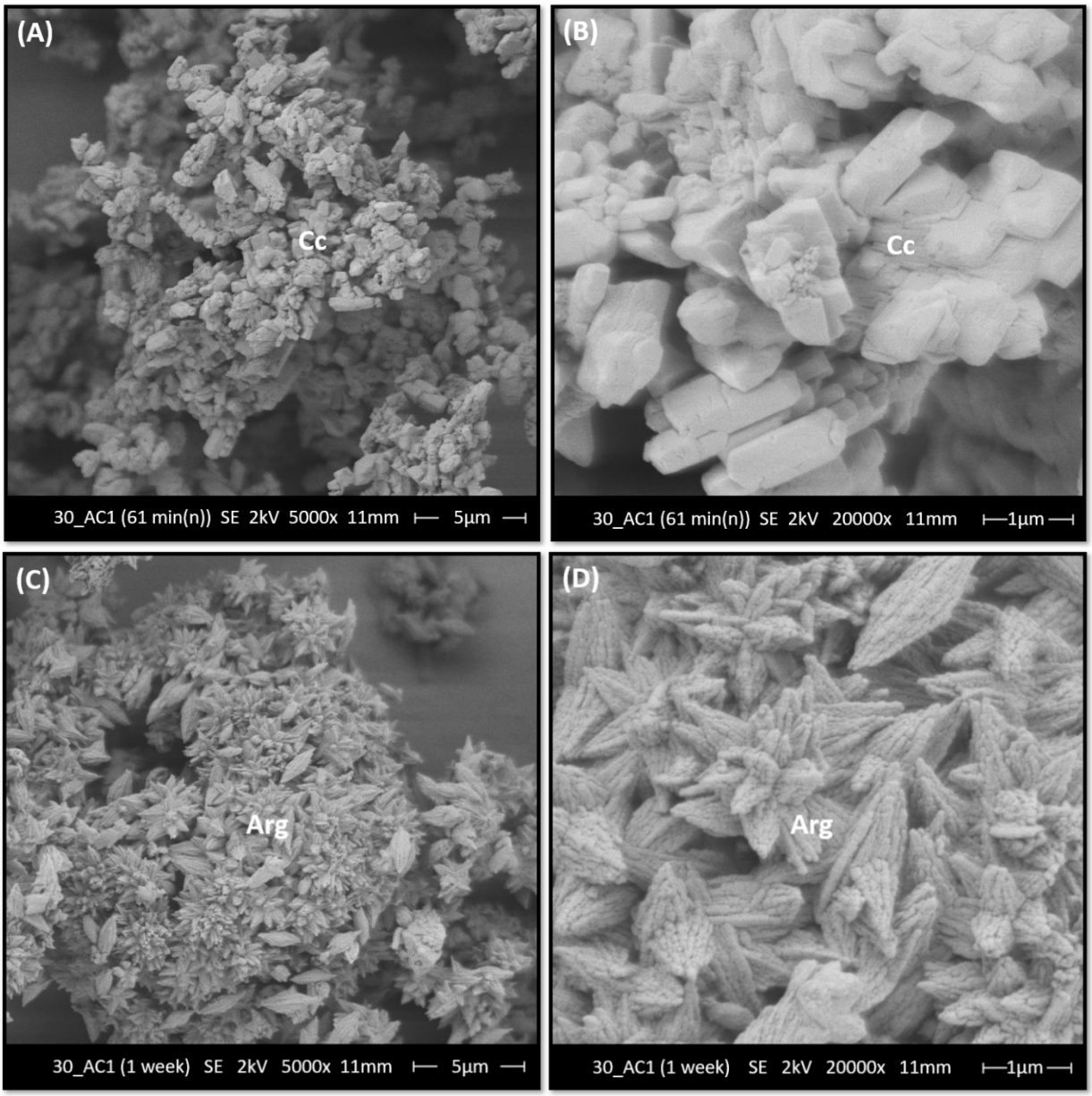

Fig. 11: SEM images of dried precipitates with different magnifications. (A - B) Cc-crystals formed in 30_AC1 after one month (61 min(n)) of reaction time. (C - D) Arg-crystals formed in 30_AC1 after one week of reaction time.

In experiment 30_AC10a, the transformation of the ACC took place after ~30 min (Fig. 12). Similar to experiment Mg50, a v_1 band at ~1101 cm^{-1} and a weak v_4 band at ~700 cm^{-1} indicate the formation of CCHH**.** After one week of reaction time, CCHH was no longer present in the solution, but Raman bands at ~1085 cm^{-1} (v_1) and at ~705 cm^{-1} (v_4) were shown, which suggest the formation of Arg **(Kontoyannis and Vagenas, 2000).**

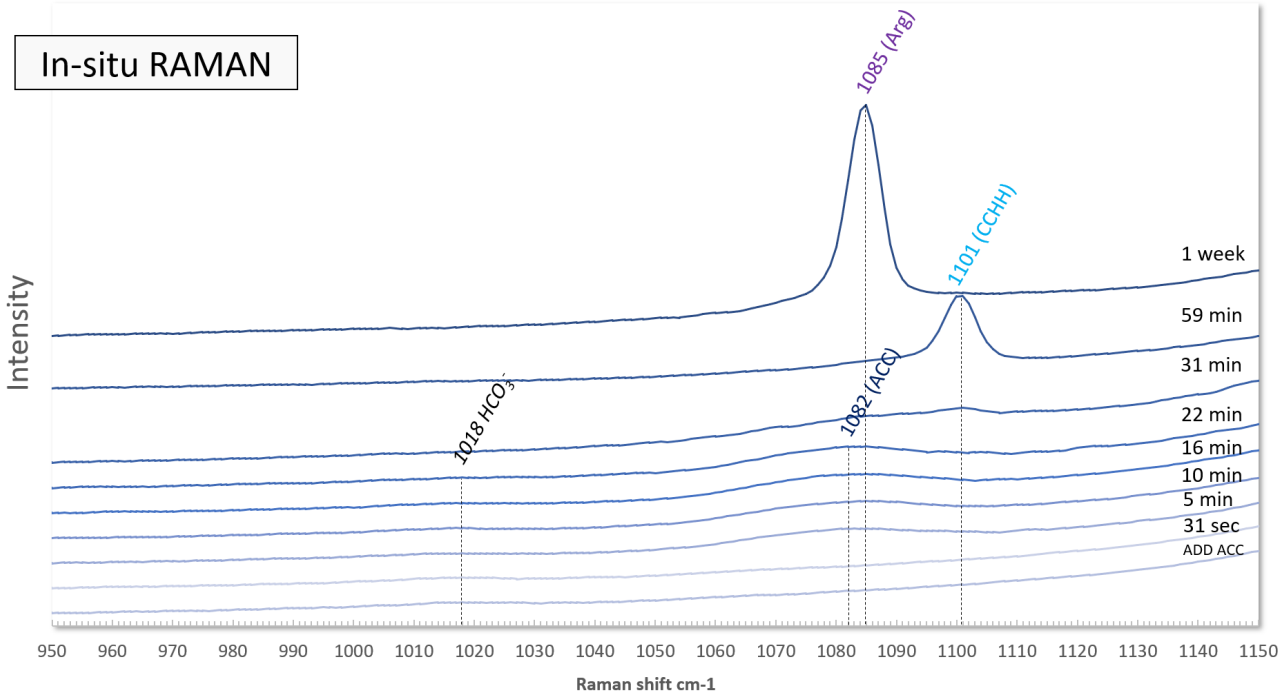

Fig. 12: In-situ Raman spectra from 30_AC10a showing the temporal evolution of mineral precipitation of ACC, CCHH and Arg.

The characteristic peaks of CCHH were recognized in the XRD pattern of the reaction product collected at 59 min (Fig. 13). The precipitates collected after one week, however, showed solely Arg (Fig. 13).

The presence of CCHH, after 59 min of reaction time could also be confirmed using ATR-FTIR by bands at ~1096 cm^{-1}, v_2 at ~860 cm^{-1} and v_4 at ~692 cm^{-1} **(Zou et al., 2019).** ATR-FTIR spectra of samples collected after one week showed only Arg, recognizable by the characteristic bands v_1 at ~1083 cm^{-1}, v_2 at ~854 cm^{-1} and v_4 at ~700 cm^{-1} and ~713 cm^{-1} **(Andersen and Brečević, 1991).**

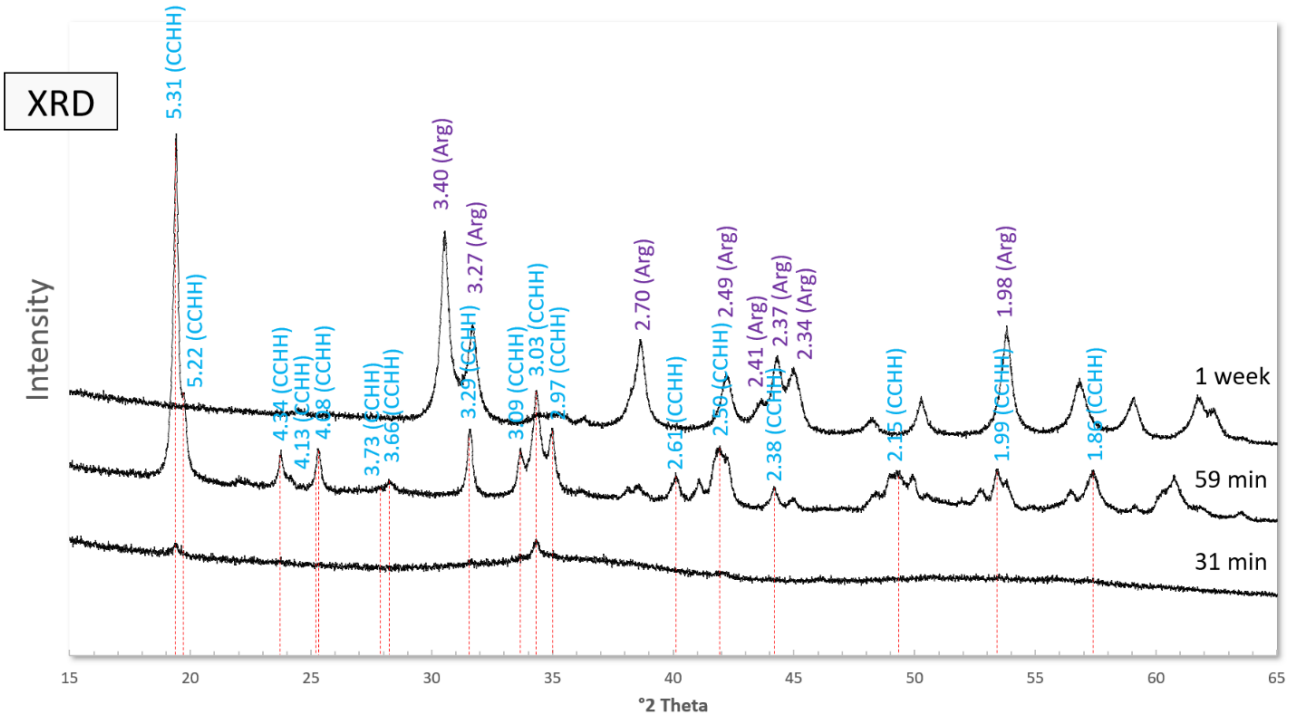

*Fig. 13: XRD spectrum of 30_AC10a after 31 min of reaction time indicates the precipitation of CCHH. The dashed red lines indicate the XRD peaks of CCHH identified by **Zou et al. (2019)** compared to the CCHH peaks after 59 min of reaction time (blue values) and XRD Arg peaks after one week of reaction time (purple values) (Ref. Code: 98-000-5272).*

The SEM images of the 30_AC10a precipitates collected after one week of reaction time showed the same Arg that formed ~100 - 300 nm crystals aggregating into ~2 - 5 µm sized rods, as in experiment 30_AC1. Furthermore, AC particles with a diameter of 2 - 5 µm were found in the sample (Fig. 14).

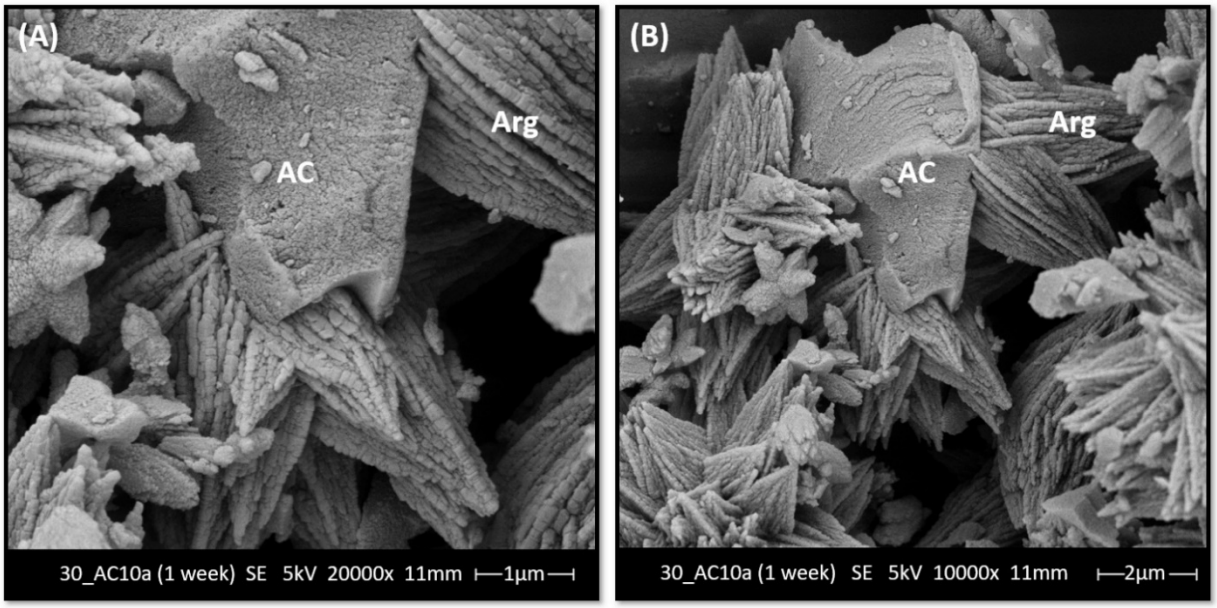

Fig. 14: SEM images of dried precipitates with different magnifications. Arg-crystals were formed beside the AC particles after one week of reaction time in the experiment 30_AC10a.

Experiment 30_AC10b was carried out under identical conditions as experiment 30_AC10a (Table 1) and was used to determine whether the same mineralogical formation paths resulted under the same initial conditions. Furthermore, additional samples were collected in the reaction period between 60 min and one week in order to be able to better understand the reaction path from CCHH to Arg, as it could be seen in experiment 30_AC10a.

Despite the same initial conditions as in experiment 30_AC10a, the transformation of the ACC into CCHH in experiment 30_AC10b starts at a later point in reaction time, as indicated by the rise of a v_1 band at ~1101 cm^{-1} and a weak v_4 band at ~700 cm^{-1} at 60 min of reaction time. After a reaction period of 102 min, bands in the area ~208 cm^{-1} (libration mode), ~1068 cm^{-1} (v_1) and ~699 cm^{-1} (v_4) became visible, which suggested the formation of Mhc beside CCHH.

From a reaction period of 24 hours, the formation of Arg, recognizable by a characteristic v_1 band at ~1085 cm^{-1} and a v_4 band at ~700 cm^{-1}, became visible in the in-situ Raman spectrum, while CCHH was no longer present in the solution. Mhc and Arg remained stable until the end of the experiment after one week (Fig. 15).

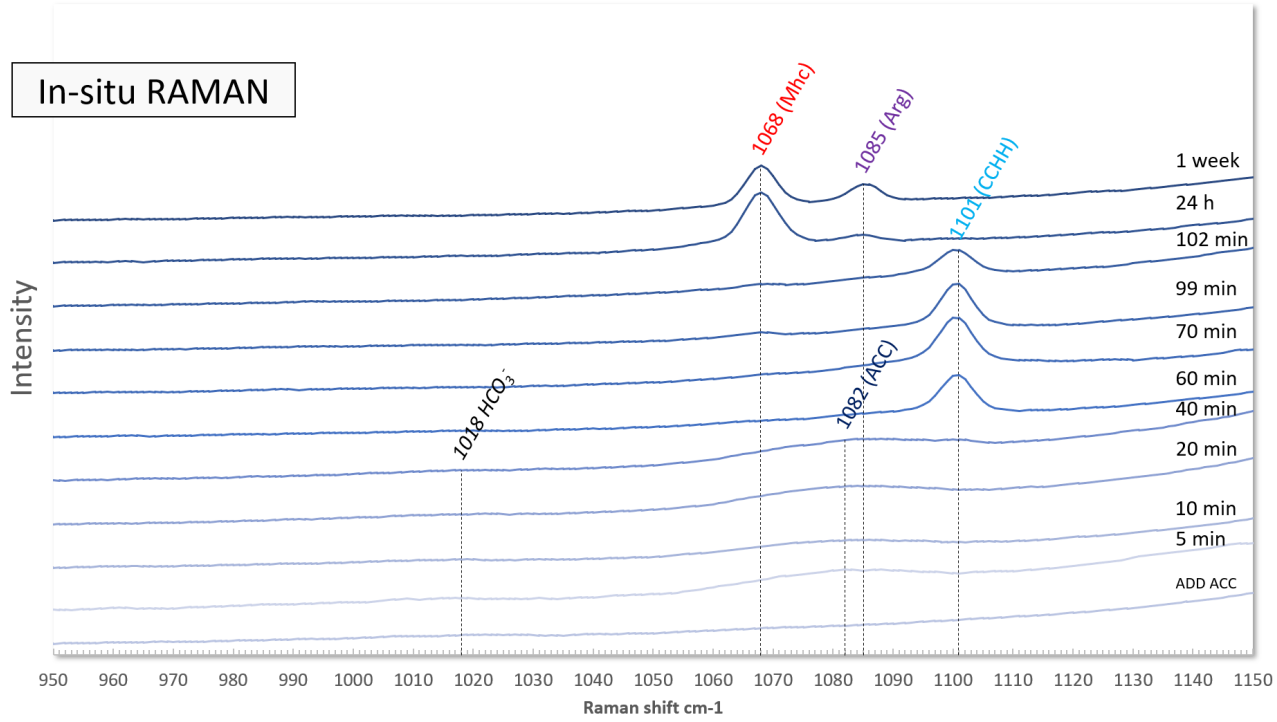

Fig. 15: In-situ Raman spectra from 30_AC10b showing the temporal evolution of mineral precipitation.

The formation of the crystalline carbonate phases, which were shown by the in-situ Raman spectra, could also be confirmed by XRD. CCHH was detected in the XRD pattern of the reaction products collected between 60 and 101 min, while Mhc, Arg and traces of nesquehonite (Nes) were detected in the samples collected after 24 hours and one week (Fig. 16). Note that the presence of Mhc in the sample collected after 102 min could not be identified beyond doubt due to the overlapping of the characteristic peaks of Mhc by those of CCHH.

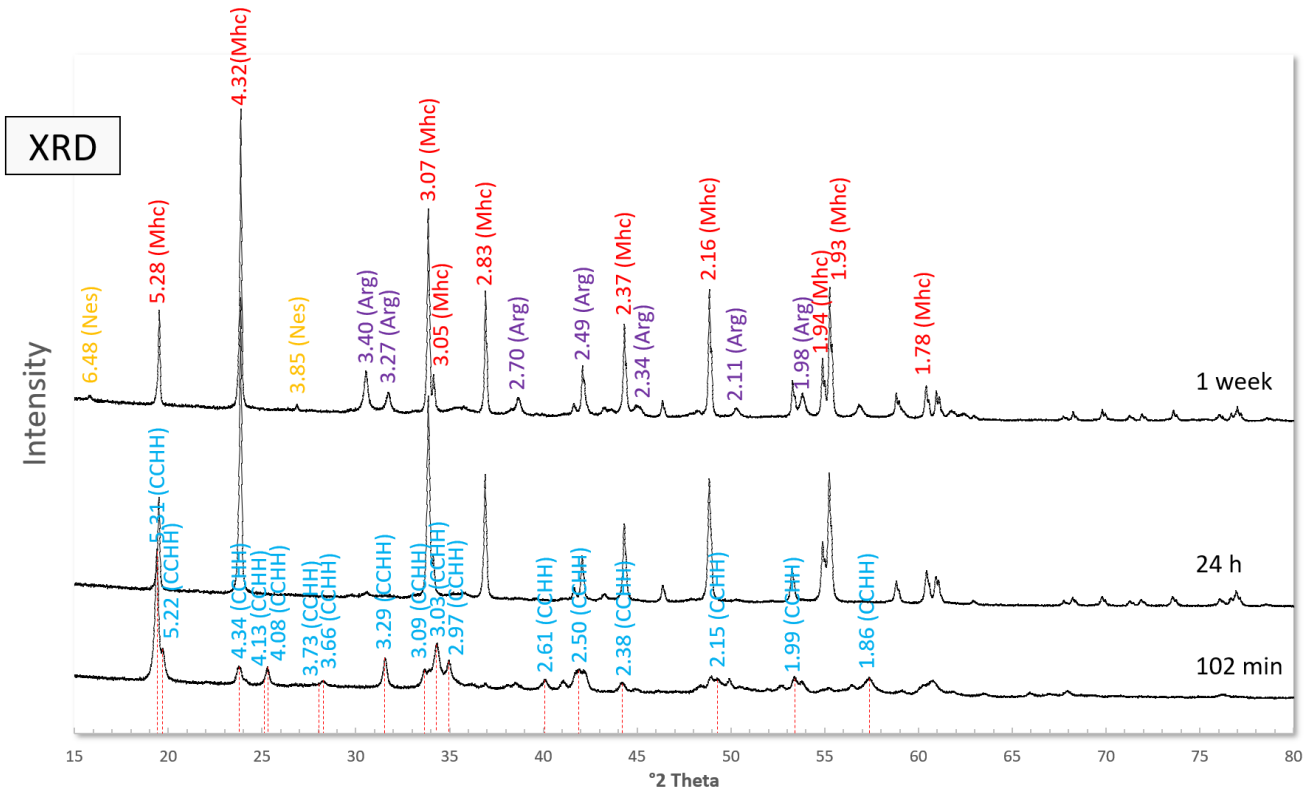

*Fig. 16: XRD CCHH peaks identified by **Zou et al. (2019)** (dashed lines in red) compared to the CCHH peaks (blue values) of precipitates of 30_AC10b sampled after 102 min of reaction time. Mhc peaks (red values; Ref. Code: 98-004-5725) and Arg peaks (purple values; Ref. Code: 98-000-5272) of precipitates collected after 24 h of reaction time. Mhc peaks, Arg peaks and Nes peaks (orange values; Ref. Code: 98-000-5428) of precipitates collected after one week of reaction time.*

The presence of CCHH in the samples collected between 60 min and 102 min could also be recognized by the bands ~1096 cm^{-1} (v_1), ~860 cm^{-1} (v_2) and ~692 cm^{-1} (v_4) in ATR-FTIR spectra. At 24 hours, bands ~1063 cm^{-1} (v_1), ~872 cm^{-1} (v_4) and bands ~762 / 698 cm^{-1} (v_4) where shown in the spectra, indicative of Mhc**.** In the sample collected after one week of reaction time, in addition to Mhc, the presence of Arg was also indicated in the spectrum, by the bands ~1083 cm^{-1} (v_1), ~854 cm^{-1} (v_2) and ~713 / 700 cm^{-1} (v_4) **(Andersen and Brečević , 1991).**

The SEM images of the precipitates of 30_AC10b after ~70 min of reaction time, showed the same aggregates (~1 - 2 µm) of platelet-shaped CCHH-crystals as they could already be found in experiment Mg50 (Fig. 17 A - B). Furthermore, AC particles with a diameter of 2 - 5 µm could be found in the sample collected after 70 min. The SEM images of the precipitates of 30_AC10b after one week of reaction time showed pseudo-hexagonal crystals of Arg (Fig. 17 C - D). Aggregates (~100 - 300 nm) of rhombohedral Mhc-crystals and a few aggregates (~10 - 20 µm) of euhedral needle-shaped Nes-crystals were observed in the sample collected after one week (Fig. 17 C - D).

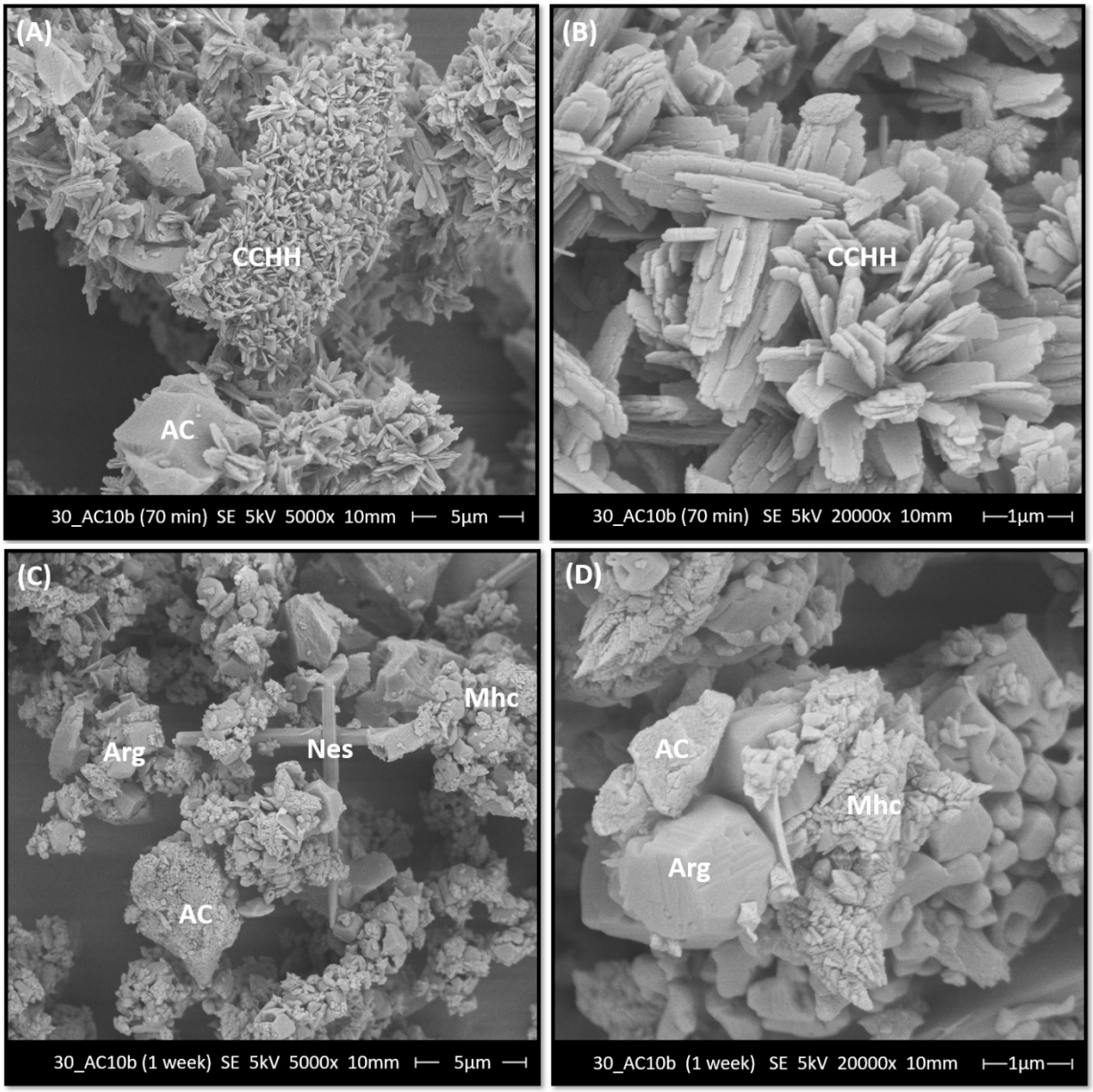

Fig. 17: SEM images of dried precipitates with different magnifications. (A - B) CCHH-crystals formed beside AC particles in 30_AC10b after 70 min of reaction time. (C - D) Arg-, Mhc- and Nes-crystals formed beside AC particles in 30_AC10b after one week of reaction time.

Table 4: Chemical composition of experimental solutions and solids of all experiments. $[Mg]_{solid\ calculated}$ was obtained by Mass balance estimate.

Experiment	time	pH	temp	0.5 M NaOH	Alkalinity	[Ca]aq	[Mg]aq	$[Mg]_{solid}$ *calculated*	$[Mg]_{solid}$ *measured*
	sec/min/h/week		*°C*	*ml*	*mM*	*mM*	*mM*	*mol%*	*mol%*
Mg50_0	0 sec	8.30	23.6	0	102.8	--	48.2	--	--
Mg50_1	18 sec	8.37	23.6	0	106.3	6.3	44.8	1.2	--
Mg50_2	9 min	8.36	23.8	0	106.3	6.4	44.2	1.4	3.0
Mg50_3	20 min	8.38	24.1	0	103.0	6.2	43.0	1.9	3.1
Mg50_4	37 min	8.42	24.4	0	99.6	5.5	44.4	1.4	3.4
Mg50_5	50 min	8.42	24.8	0	97.2	5.1	42.8	1.9	3.8
Mg50_6	63 min	8.46	25.0	0	95.0	4.6	41.4	2.4	3.7
Mg30_0	0 sec	8.39	22.9	0	98.4	--	28.8	--	--
Mg30_1	56 sec	8.38	23.1	0	105.8	6.1	26.9	0.7	2.3
Mg30_2	5 min	8.38	23.1	0	107.2	6.0	26.7	0.8	2.7
Mg30_3	10 min	8.38	23.4	0	104.8	5.7	25.7	1.1	2.2
Mg30_4	16 min	8.30	24.1	0.12	100.8	5.6	22.3	2.3	3.4
Mg30_5	21 min	8.29	24.5	1.74	72.9	2.4	5.6	7.7	8.2
Mg30_6	30 min	8.35	24.8	2.04	63.3	0.5	1.6	8.9	9.6
Mg30_7	60 min	8.62	25.2	2.04	74.2	0.2	1.2	9.0	9.4
30_AC1_0	0 sec	8.12	21.5	0	100.4	--	30.4	--	--
30_AC1_1	22 sec	8.44	21.6	0	103.9	5.3	29.4	0.3	3.9
30_AC1_2	6 min	8.44	21.8	0	103.0	5.0	28.1	0.8	2.5
30_AC1_3	11 min	8.46	22.0	0	99.0	5.1	27.2	1.1	2.3
30_AC1_4	21 min	8.50	22.3	0	102.4	4.6	27.1	1.2	2.4
30_AC1_5	30 min	8.52	22.5	0	95.6	4.0	26.3	1.5	2.6
30_AC1_6	61 min	8.59	23.1	0	84.7	1.0	21.7	3.0	3.9
30_AC1_7	24 h	8.69	21.9	0	75.4	0.1	15.8	5.0	6.0
30_AC1_8	1 week	8.85	21.7	0	70.4	0.1	14.0	5.5	6.6
30_AC10a_0	0 sec	8.51	21.3	0	101.5	--	29.5	--	--
30_AC10a_1	31 sec	8.51	21.3	0	104.7	4.9	27.3	0.8	2.8
30_AC10a_2	5 min	8.52	21.6	0	102.1	5.1	26.7	1.0	2.5
30_AC10a_3	10 min	8.54	21.8	0	101.3	4.8	26.5	1.1	2.5
30_AC10a_4	16 min	8.56	22.0	0	104.1	4.6	26.2	1.2	2.7
30_AC10a_5	22 min	8.58	22.2	0	101.9	4.5	26.0	1.2	2.6
30_AC10a_6	31 min	8.58	22.6	0	99.2	4.1	25.6	1.4	2.7
30_AC10a_7	59 min	8.72	23.2	0	93.7	1.7	24.2	1.8	3.0
30_AC10a_8	1 week	8.77	21.7	0	76.2	0.1	18.8	3.7	4.5
30_AC10b_1	5 min	8.52	22.2	0	104.2	4.7	27.4	0.6	2.6
30_AC10b_2	10 min	8.53	22.3	0	102.0	4.6	28.1	0.3	2.6
30_AC10b_3	20 min	8.57	22.7	0	99.7	4.4	27.5	0.5	2.5
30_AC10b_4	40 min	8.67	23.1	0	96.0	3.3	26.3	1.0	3.2
30_AC10b_5	60 min	8.79	23.8	0	91.9	1.6	24.5	1.6	3.7
30_AC10b_6	70 min	8.84	23.8	0	93.5	1.1	24.1	1.7	3.6
30_AC10b_7	99 min	8.92	23.7	0	91.7	0.6	23.6	1.9	3.7
30_AC10b_8	102 min	8.93	23.8	0	92.8	0.6	23.4	2.0	3.4
30_AC10b_9	24 h	9.10	22.8	0	105.1	0.1	19.3	3.3	4.6
30_AC10b_10	1 week	9.15	22.6	0	94.4	0.1	12.8	5.5	7.5

4.2. Chemical composition of the reactive solutions

The initial solution exhibits a pH of 8.4 ± 0.1 and alkalinity concentration of 101 ± 3 mM (without 30_AC10a). The initial Mg-concentration ($[Mg]_{aq}$) is 48 ± 1 mM in experiment Mg50 and 29 ± 1 mM in experiment Mg30, 30_AC1, 30_AC10a and 30_AC10b (Table 4). The dispersion of ACC into the $NaHCO_3$ - $MgCl_2$ solution leads to a rapid and slight increase of the Ca concentration ($[Ca]_{aq}$), alkalinity concentration and pH of the reactive solution (Table 4), originating from the dissolution of ACC. In contrast, the initial $[Mg]_{aq}$ decreased slightly as soon as the ACC was dispersed into the reactive solution (Table 4). The ACC dissolved in the reactive solution until the solution reached saturation (SI_{ACC} = 0.23 ± 0.03) with respect to this phase (Table 5). Note here that the slight supersaturation (> 0) with respect to ACC is caused by Mg-incorporation into the ACC, which is not considered for the SI calculations by the PHREEQC *MINTEQ.V4* database. The solubility of Mg-rich ACC increases as a function of mg content which is leading to slightly higher SI values **(Purgstaller et al., 2019).**

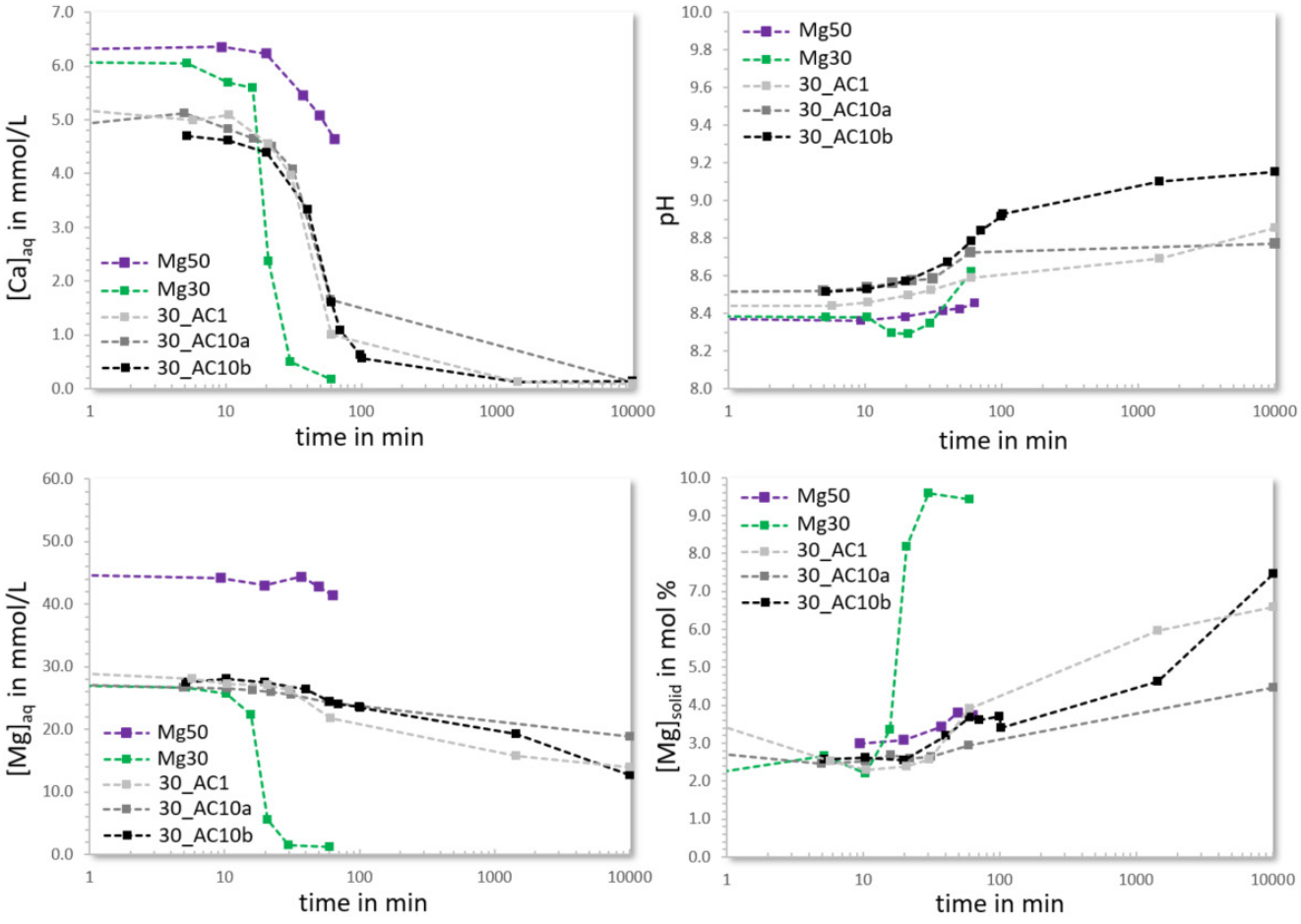

Fig. 9: (Left) Concentration of dissolved Ca and Mg ions of all reactive solutions, $[Ca]_{aq}$ and $[Mg]_{aq}$, over a certain reaction time. (Right) pH of all reactive solutions over a certain reaction time and Mg-content of the precipitated solids, $[Mg]_{solid}$.

Subsequently, the data show an overall decrease of the $[Ca]_{aq}$, a slight decrease of the $[Mg]_{aq}$ (Fig. 18) and an overall decrease of the alkalinity concentration (Table 4) as a function of reaction time, which can be attributed to the transformation of ACC into the crystalline carbonate phase. Note that the decrease of the $[Ca]_{aq}$, $[Mg]_{aq}$ and alkalinity concentration occurs earlier in the experiment where ACC transformed into Mg-Cc (Mg30) than in the experiments where ACC transformed into CCHH (Mg50, 30_AC1, 30_AC10a and 30_AC10b) (Table 4; Fig. 18).

4.3. Evolution of mineralogical and solid Mg-content

Two reaction pathways could be observed in all experiments. Reaction pathway (A) in which ACC first transformed into CCHH and reaction pathway (B) in which ACC transformed into Mg-Cc. The reaction pathway (A) is divided into two different reaction pathways, in which the ACC is first transformed into (1) a recently discovered thermodynamically metastable intermediate phase CCHH **(Zou et al., 2019)**, or (2) two intermediate phases CCHH and Mhc, before the final polymorph Arg was formed in both cases of reaction pathway (A) (Table 3). When reaction pathway (A) occurred, no additional titration of 0.5 NaOH was necessary during the transformation from ACC to CCHH and / or Mhc in order to keep the pH constant. With ongoing reaction time - after the ACC transformation - there was possibly a slight increase in pH due to the degassing of CO_2. However, when the reaction pathway (B) occurred, the automatic titration of NaOH during the transformation from ACC to Mg-Cc ensured almost steady pH values of 8.35 ± 0.03 but would have resulted in a rapid decrease in pH without the titration of NaOH (Table 4), due to a very high precipitation rate.

The Mg-composition of the collected solids ($[Mg]_{solid}$ in mol%) is reported in Table 4. As mentioned above, the initial $[Mg]_{aq}$ decreased slightly as soon as the ACC was dispersed into the $NaHCO_3$ - $MgCl_2$ solution. The uptake of Mg from the solution into the solids resulted in the formation of Mg-containing ACCs with Mg-contents that were difficult to determine in those experiments where AC was used.

In the reactive solutions of Mg50, 30_AC1, 30_AC10a and 30_AC10b, where ACC transformed into CCHH, a slight decrease in the $[Mg]_{aq}$ (Fig. 18) was observed over the remaining reaction time up to one week. Simultaneously there was an increase in the $[Mg]_{solid}$ which continued until the formation of Arg and afterwards. Therefore, the final samples which mainly consisted of Arg, showed uncommonly high $[Mg]_{solid}$ contents up to ~6.6 mol% Mg (Fig. 18; Table 4).

In comparison, there was a significant decrease in the $[Mg]_{aq}$ in the reactive solutions of experiment Mg30 due to the formation of Mg-Cc via ACC, at the reaction time when Mg-Cc was formed, the $[Mg]_{solid}$ increased rapidly and resulted after ~60 min finally in Mg-Cc containing ~7.7 ± 1mol% Mg, calculated from the d_{104} according to **Goldsmith et al. (1961)**.

Table 5: Calculated aMg^{+2}/aCa^{+2} ratios and molar Mg/Ca ratios of aqueous species as well as saturation indices (SI). Therefore, the PHREEQC software and edited MINTEQ.V4 database was used.

Sample	**time** *sec/min/week*	**aMg^{+2}/aCa^{+2}** *calculated*	**molar Mg/Ca** *measured*	**SI_{ACC}**	**SI_{Mhc}**	**SI_{Arg}**	**SI_{Cc}**	**SI_{Nes}**	**SI_{Bru}**
Mg50_0	0 sec	--	--	--	--	--	--	--	--
Mg50_1	18 sec	8.7	7.1	0.23	1.05	2.13	2.32	0.02	-2.20
Mg50_2	9 min	8.5	7.0	0.22	1.05	2.13	2.31	0.01	-2.22
Mg50_3	20 min	8.4	6.9	0.23	1.05	2.13	2.32	0.02	-2.16
Mg50_4	37 min	9.9	8.1	0.18	1.01	2.09	2.27	0.04	-2.07
Mg50_5	50 min	10.3	8.4	0.16	0.98	2.07	2.25	0.04	-2.04
Mg50_6	63 min	10.9	8.9	0.14	0.96	2.05	2.23	0.05	-1.98
Mg30_0	0 sec	--	--	--	--	--	--	--	--
Mg30_1	56 sec	5.5	4.4	0.25	1.08	2.15	2.34	-0.16	-2.43
Mg30_2	5 min	5.4	4.4	0.25	1.08	2.15	2.34	-0.16	-2.44
Mg30_3	10 min	5.6	4.5	0.22	1.05	2.13	2.31	-0.17	-2.44
Mg30_4	16 min	4.9	4.0	0.15	0.98	2.06	2.24	-0.29	-2.61
Mg30_5	21 min	2.8	2.4	-0.26	0.56	1.64	1.82	-0.94	-3.14
Mg30_6	30 min	3.8	3.2	-0.92	-0.10	0.99	1.17	-1.47	-3.55
Mg30_7	60 min	8.6	6.7	-1.12	-0.31	0.78	0.96	-1.31	-3.15
30_AC1_0	0 sec	--	--	--	--	--	--	--	--
30_AC1_1	22 sec	6.8	5.6	0.21	1.05	2.11	2.30	-0.12	-2.38
30_AC1_2	6 min	6.9	5.6	0.19	1.03	2.09	2.28	-0.13	-2.38
30_AC1_3	11 min	6.5	5.3	0.20	1.04	2.11	2.30	-0.13	-2.34
30_AC1_4	21 min	7.4	6.0	0.19	1.03	2.10	2.29	-0.09	-2.26
30_AC1_5	30 min	8.2	6.6	0.14	0.98	2.05	2.23	-0.09	-2.20
30_AC1_6	61 min	27.0	21.8	-0.42	0.41	1.48	1.67	-0.14	-2.10
30_AC1_7	24 h	152.8	123.0	-1.27	-0.42	0.64	0.83	-0.23	-2.10
30_AC1_8	1 week	195.1	154.3	-1.33	-0.49	0.57	0.76	-0.19	-1.86
30_AC10a_0	0 sec	--	--	--	--	--	--	--	--
30_AC10a_1	31 sec	6.9	5.6	0.23	1.08	2.14	2.33	-0.09	-2.29
30_AC10a_2	5 min	6.4	5.2	0.25	1.10	2.16	2.35	-0.09	-2.27
30_AC10a_3	10 min	6.8	5.5	0.24	1.08	2.15	2.34	-0.08	-2.22
30_AC10a_4	16 min	7.1	5.6	0.25	1.09	2.16	2.35	-0.05	-2.17
30_AC10a_5	22 min	7.2	5.8	0.24	1.08	2.15	2.34	-0.05	-2.13
30_AC10a_6	31 min	7.9	6.3	0.20	1.04	2.11	2.29	-0.05	-2.10
30_AC10a_7	59 min	18.7	14.7	-0.11	0.72	1.80	1.98	0.02	-1.81
30_AC10a_8	1 week	183.4	147.0	-1.23	-0.39	0.68	0.87	-0.12	-1.90
30_AC10b_1	5 min	7.3	5.8	0.22	1.06	2.13	2.32	-0.07	-2.23
30_AC10b_2	10 min	7.6	6.1	0.22	1.06	2.12	2.31	-0.05	-2.18
30_AC10b_3	20 min	7.8	6.3	0.22	1.06	2.13	2.32	-0.03	-2.08
30_AC10b_4	40 min	10.0	7.9	0.17	1.00	2.08	2.26	0.03	-1.87
30_AC10b_5	60 min	19.8	15.3	-0.09	0.74	1.82	2.00	0.07	-1.65
30_AC10b_6	70 min	29.1	22.2	-0.22	0.61	1.69	1.87	0.11	-1.56
30_AC10b_7	99 min	49.3	37.2	-0.42	0.41	1.49	1.67	0.14	-1.43
30_AC10b_8	102 min	55.8	42.0	-0.46	0.37	1.45	1.63	0.15	-1.40
30_AC10b_9	24 h	229.9	164.0	-1.03	-0.20	0.88	1.06	0.19	-1.26
30_AC10b_10	1 week	124.0	88.4	-0.93	-0.10	0.98	1.16	0.02	-1.35

5.Discussion

5.1. Overall reaction pathways

The present ACC transformation experiments which were performed at 23 ± 1 °C and pH 8.5 ± 0.2 with 50 mM and 30 mM (with / without additions of 1 wt.% AC and 10 wt.% AC) of total aqueous Mg^{2+} reactive solution, revealed reaction pathways in which (A) the anhydrous polymorph Arg, or (B) the anhydrous polymorph Mg-Cc, were formed as the final reaction products from ACC (Fig. 19).

In the experiments of our study, a similar trend of increased Mg-incorporation into ACC (reliable values only in the experiments Mg50 and Mg30 without using AC), as well as an increased metastability of the amorphous phase, could be observed at increased initial molar Mg/Ca ratio, similar as it was observed in the study by **Konrad et al., 2018** (Fig. 20; Table 3). Note here, that in all experiments brucite (Bru; $SI_{Bru} < 0$) was strongly undersaturated (Table 5). Furthermore, no characteristic Bru OH-stretching band (~3700 cm^{-1}) could be determined in the ATR-FTIR spectra. Therefore, the formation of Bru during reaction times of the experiments can be excluded.

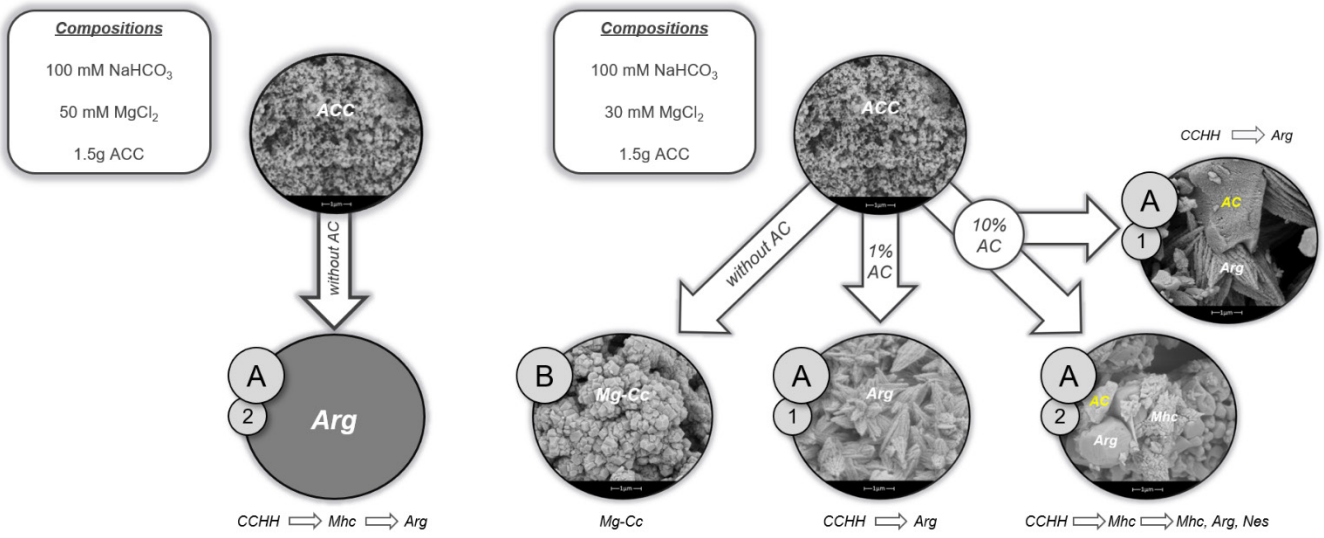

Fig. 10: Observed reaction pathways (A + B; 1 + 2) in experiments carried out with 50 mM MgCl2 in the reactive solution (left) and with 30 mM $MgCl_2$ of the reactive solution (right) in absence and presence of AC.

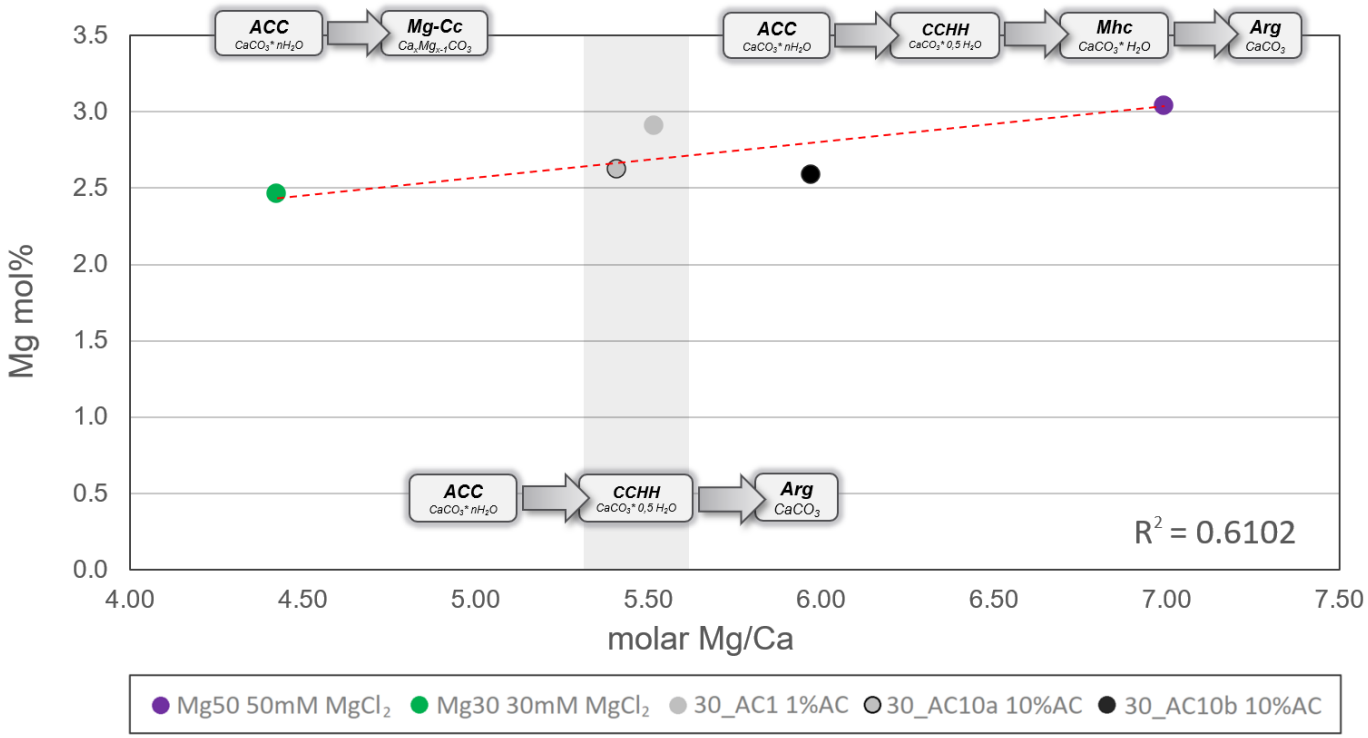

Fig. 11: Average Mg-incorporation (Mg mol%) into ACC versus average molar Mg/Ca ratios in the initial phases of all experiments. The dashed red line marks the increase in Mg-incorporation with an increase in the molar Mg/Ca ratio.

5.1.1. Mg-Cc formation

The experiment Mg30 was the only one in which the formation of Mg-Cc could be detected, see pathway (B) in Fig. 19. The ACC in Mg30 showed the lowest metastability (~16 min) observed in our study, which could be explained by the fact, that Mg-Cc formation is a process that is generally initiated earlier compared to e.g. Mhc formation **(Purgstaller et al., 2017)**. Mg-Cc formation typically reveals a high $CaCO_3$ precipitation rate which can be traced by a rapid decrease of pH as could be observed in Mg30 (Fig. 18). The initial aMg^{2+}/aCa^{2+} ratio and the initial molar Mg/Ca ratio were the lowest in the experiment Mg30 (Table 5). In experiments of **Purgstaller et al. (2017)**, they observed formation of the Mg-Cc at very similar initial ratios and pH conditions, which showed the same rhombohedral crystal morphology (Fig. 8). Note here, that the above molar Mg/Ca ratio is similar to those in today´s seawater (molar Mg/Ca ratio of ~5.2), in which Mg-rich Cc formation (e.g. marine Calcite cements) is documented **(Mackenzie et al., 1983).**

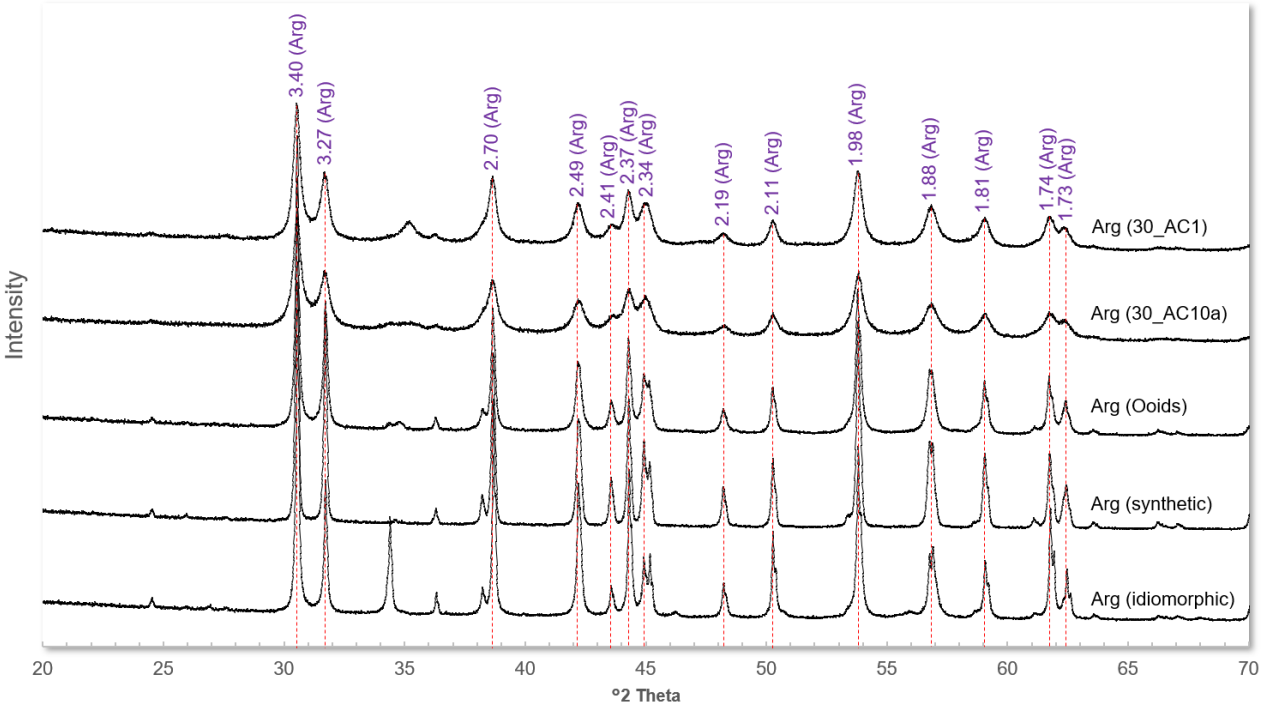

Fig. 12: Various XRD-spectra of Arg-standards (idiomorphic (92.2% Arg, 7.8% Cc, Hüttenberg); synthetic (100% Arg); Ooids (100% Arg)) plotted against XRD-spectra of Arg (30_AC1, 30_AC10a) obtained in the present study. The dashed red lines indicate the characteristic Arg peaks (Ref. Code: 98-000-5272).

5.1.2. Arg formation

The formation of Arg revealed two different ACC transformation pathways in which the amorphous phase first transformed into (i) a recently discovered thermodynamically metastable intermediate phase CCHH **(Zou et al., 2019)**, or (ii) two intermediate phases CCHH and Mhc, before the Arg was finally formed (Table 3).

In the experiments by **Zou et al. (2019)**, it has been observed that the orthorhombic CCHH can be formed via the Mg-containing ACC, whereby a minor amount of the magnesium remains incorporated in the structure of CCHH. They also observed the transformation of CCHH into hydrous Mhc, which, as already mentioned, is characterized by a slower formation process compared to the formation of anhydrous Cc. This may lead to co-precipitation of another, also recently discovered, hydrated $CaCO_3$ phase with ¾H_2O in its structure and a platelike morphology **(Zou et al., 2019).**

A similar platelike morphology was also observed in our SEM images of those CCHH subsamples, where the intermediate phase Mhc was subsequently formed (Mg50, 30_AC10b). The ordinary needle-shaped CCHH morphology could not be observed in any subsample of Mg50 and 30_AC10b which suggests that the platelike CCHH observed by SEM (Fig. 5 and Fig. 17) can be likely ascribed to the mineral phase containing ¾ H_2O instead of ½ H_2O. This $CaCO_3$ • ¾H_2O phase is poorly described in the literature but seemingly structurally interrelated with CCHH **(Zou et al., 2019).** It is most likely that due to the thermodynamic metastability of CCHH, a transformation already occurred between sampling and its analysis and therefore only the platelike morphology of $CaCO_3$ • ¾H_2O could be observed.

It is known that the anhydrous Arg, as well as the hydrated intermediate phases Mhc and Nes, are formed from aqueous solutions at high molar Mg/Ca ratios **(Konrad et al., 2018)**, in which the high Mg^{2+} concentration leads to poisoning of active growth sites of Cc´s pre-critical nuclei by attaching hydrated Mg ions onto its surfaces **(Fernández-Díaz et al., 1996).** Poisoning by Mg^{2+} ions significantly slows down the Cc growth rate during crystallization and inhibits its nucleation / formation **(Aufort and Demichelis, 2020).**

Zou et al. (2019) observed, that at a high Mg-concentration (molar Mg/Ca ratio of ~5; pH ≥ 10.5) the Cc formation in a reactive solution is inhibited and the formation of CCHH, which fits well with the observations from our study in which the lowest initial molar Mg/Ca ratio of ~4.4 resulted in the absence of CCHH and the formation of Mg-Cc (Table 5). However, CCHH was detected in all of our experiments where the finally Arg was formed (Table 3). Since some of the Arg samples showed increased $[Mg]_{solid}$ values (Fig. 18), we suggested an atypically high Mg-incorporation into its structure when Arg is formed via the transient CCHH phase.

For a previous approach to explain the high $[Mg]_{solid}$ values in the final Arg samples, we considered the adsorption of ions on AC. However, experiments with different proportions of AC (e.g. 1 wt.% vs. 10 wt.%) did not reveal any significant differences in the Mg-contents of the final solids, which is why direct Mg incorporation in the Arg structure is possible (Table 4; Fig. 18).

The incorporation of magnesium into the orthorhombic structure of Arg is rarely observed, since Mg^{2+} is only sixfold coordinated and Ca^{2+} is ninefold coordinated in respect to oxygen ions in Arg. Therefore, Mg^{2+} is unlikely substituted for Ca^{2+} in its lattice **(Wang et al., 2013).** Nevertheless, the Mg-incorporation in Arg is commonly observed in aragonitic corals **(Ruiz-Hernandez et al. 2012)** and was justified based on experiments and molecular dynamics simulations **(Yao et al., 2019)**, but still a matter of hot debate in respect to the potential position of Mg ions in the Arg structure.

In the experiments by **Yao et al. (2019)**, it has been observed that the presence of organic additives (polysaccharides) in the reactive solution, as well as a significant increase of the mineralization temperature and the molar Mg/Ca ratio, can lead to an increased Mg-incorporation into Arg. They suggested that the Mg-content in Arg could be influenced by the presence of biomolecules, locally defective substitution or complex adsorption onto its crystal surface, thus similar as induced herein by ACC as intermediate phase known to be valid for biomineralization strategies.

In the study of **Németh et al.**, for the first time the monoclinic Arg (mAra) was postulated as a fourth anhydrous $CaCO_3$ polymorph, which is suggested to be a precursor phase of Arg and is formed among others by the Mg-incorporation into its low-coordination cation sites. During the growth of mAra, Mg^{2+} is released back into the aqueous solution and mAra is gradually transformed into the orthorhombic Arg. Since up to 10 atomic% Mg can be replaced in mAra, the Mg^{2+} may “remain” partly incorporated in the $CaCO_3$ during its transformation to Arg **(Németh et al., 2018).**

In order to determine any differences, we compared some of the obtained Arg samples (30_AC1, 30_AC10a), with well-known Arg-standards by using FTIR spectra, as well as XRD spectra which were quantified using Rietveld refinement (PANalytical X´Pert HighScore Plus software; PDF-2 database; Fig. 21) **(Purgstaller et al., 2016).**

Lattice parameters showed no significant differences. However, XRD spectra of our Arg precipitates showed broadened peaks with weaker intensities (Fig. 21), which indicates the formation of nanosized crystals and poorly crystalline minerals **(Ungár, 2004; Xto et al., 2019),** which fits well with the nanocrystalline Arg morphology we observed (Fig. 11). Therefore, we suggest that the high Mg-content we observed in our Arg samples, likely reflects substitution of locally occurring defective crystal sites **(Yao et al., 2019).**

Interestingly, in some of the final Arg samples (Mg50, 30_AC1; Table 3), the presence of minor proportions of Cc - as detected by XRD pattern - was not confirmed by any other solid characterization methods (e.g. ATR-FTIR). It is known that Arg transforms into Cc at some point, since Arg is less thermodynamically stable phase compared to Cc **(Aufort and Demichelis, 2020; Okrusch and Matthes, 2014).** This transformation process could have been triggered by artificial effects during preparation of the samples (e.g. drying process, crushing and grinding) **(Okrusch and Matthes, 2014).**

In transformation experiments, where only the formation of the metastable intermediate phase CCHH could be observed (30_AC1, 30_AC10a), revealed very strong similarities in pH (~8.5 ± 0.1), temperatures (21.6 ± 0.2 °C), aMg^{2+}/aCa^{2+} ratios of ~6.7 and molar Mg/Ca ratios of ~5.5 in the initial phases of the experiments (Table 5). ACCs which could be observed during those phases, showed similarities in metastability (30.5 ± 0.5 min). The nanocrystalline Arg morphology observed in 30_AC1 and 30_AC10a, showed very strong similarities to the morphology of experiments by **Konrad et al. (2018)**, in which they observed the formation of Nes and Mhc as intermediate phases during Arg formation from a $MgCl_2$-rich solution.

The increased Mg-incorporation in the final samples could be ascribed to the nanocrystalline Arg morphology (Fig. 18), which could be detected as its only solid phase (Table 3), since it is known that the Mg-incorporation in Arg happens by locally defective substitution **(Yao et al., 2019).** The observed nanocrystalline Arg morphology could be predestined for this type of substitution. Furthermore, the incorporation of Mg^{2+} could have caused a lattice distortion in the Arg.

The principle of lattice distortion through ion substitution in Cc-crystals and the resulting variety of Cc morphology is well known **(Morse and Mackenzie, 1990).** Since Mg^{2+} is hardly substituted due to its adverse coordination in Arg, lattice distortions in Arg are poorly known. However, since the increased incorporation of Mg^{2+} into the Arg structure could be demonstrated in a recent study, such lattice distortions could possibly occur in some cases **(Yao et al., 2019).**

In experiments Mg50 and 30_AC10b, where the formation of metastable intermediate phases CCHH and Mhc occurred and Arg was the final precipitate, ACC exhibited the longest observed metastability of 45 ± 5 min, which could be explained by (i) high initial aMg^{2+}/aCa^{2+} ratios of ~6.5 and molar Mg/Ca ratios of ~8.0 (Table 5) of the reactive solutions **(Konrad et al., 2018; Purgstaller et al., 2017)** and (ii) the ion desolvation-effect of AC **(Prehal et al., 2017).** Furthermore, CCHH remained metastable the longest in these experiments before Mhc was formed, which fits well with observations from the recent study by **Zou et al. (2019)**, where an equally long stability of the CCHH phase occurred.

In case of 30_AC10b, the increased growth time during the Arg formation led to the pseudo-hexagonal morphology, which was similar to that observed in the study of **Purgstaller et al. (2017)** (Fig. 17). Whereas the formation of Nes could be detected in the final 30_AC10b sample, which is well-known to occur together with Mhc as a metastable intermediate phase during the formation of Arg **(Konrad et al., 2018)**, no evidence of Nes formation could be found in Mg50 (Table 3). This is most likely explained by the fact that (i) only small amounts of Nes below the detection limit of mineralogical analyses were present in samples of Mg50, or (ii) due to the higher initial aMg^{2+}/aCa^{2+} ratio and the higher initial Mg-concentration in Mg50, Nes was formed but transformed again during a period when no in-situ Raman monitoring was performed and was therefore overlooked, or (iii) Nes was not formed at all (Table 3). This theory fits well with the results obtained from the study by **Konrad et al. (2018)**, in which the formation of the intermediate phases Nes and Mhc during the formation of Arg were detected with ongoing reaction time when the $MgCl_2$ concentration in the reactive solution and consequently the aMg^{2+}/aCa^{2+} ratio was high **(Konrad et al., 2018).**

5.2. Impact of AC on the reaction pathway

Since reactive solutions with lower $MgCl_2$ concentrations, but the presence of AC, showed similar formation pathways as observed in the solution with elevated Mg-concentration and without AC (Table 3), we state that the specific ACC transformation pathway is significantly affected by the presence / property of AC. The ACC transformation pathway is influenced (i) by the aMg^{2+}/aCa^{2+} ratio and the molar Mg/Ca ratio of the reactive solution where AC can be reasonably suggested to have an impact on those ratios due to its well-known ion-adsorption properties **(Marsh and Rodríguez-Reinoso, 2006)** and (ii) by the ion desolvation-effect of AC **(Prehal et al., 2017)**. The dynamic interactions of these two effects are leading in experiments performed with the addition of AC to ACC reaction pathways, which are usually observed at elevated Mg-concentrations and corresponding higher aMg^{2+}/aCa^{2+} ratios. This assumption is first supported by the study of **Rostamian et al. (2014)**, where they observed that AC with a high specific surface area has the potential to adsorb Ca^{2+} stronger than Mg^{2+} on its surface and second by the study of **Prehal et al. (2017)**, where they observed a partially dehydration of dissolved ions.

The fact that despite the identical experimental conditions, slightly different reaction pathways could be observed is probably due to the fact that (i) AC does not always adsorb / desolvate the exact same number of ions on its surface due to surface irregularities and other defects **(Marsh and Rodríguez-Reinoso, 2006)** and thus AC does not always influence the aMg^{2+}/aCa^{2+} ratio in the same way, or (ii) the transformation takes place under chemical conditions which reflect a transitional zone where the formation of more than one $CaCO_3$ polymorph is possible. The sensitivity of polymorph formation to chemical conditions was shown already in earlier experimental studies **(e.g. Blue et al., 2017; Purgstaller et al., 2017).**

6. Conclusions and Outlook

Results of our study reveal that the presence of AC has a significant influence on the prevailing aMg^{2+}/aCa^{+2} ratio and molar Mg/Ca ratio of the reactive solution and consequently the transformation behavior of ACC. However, it is still unclear in which proportions the AC influences the reactive solution, since similar metastabilities of ACC as well as same reaction pathways with similar mineralogical evolutions could be observed in experiments with different AC proportions (Table 3; Fig. 20). As described in the study, (i) the adsorption of ions (especially Ca^{2+}) on the surface of AC in solution might occur randomly and is not precisely controlled which is resulting in effects of varying degree on the ACC transformation pathway, or (ii) possibly there is a transitional zone at 10 wt.% AC, where the formation of more than one $CaCO_3$ polymorph is possible ((1) and (2); Fig. 19). Another possibility, how the transformation behavior of ACC could be influenced by AC, is the ion desolvation-effect of AC, whereby Mg^{2+} and other ions are partially dehydrated, and its effectiveness is increased during the carbonate formation. To describe this system more precisely, the effect of different AC concentrations should be investigated in a series of experiments, where the addition is varied in wider range compared to the given thesis, e.g. to reveal whether the formation of nanocrystalline Arg can still be observed at higher additions of AC. In addition, the Mg-concentration in the initial reactive solution could be reduced even more, to reveal whether the formation of Mg-Cc can be observed, since AC apparently increases the molar Mg/Ca ratio in the solution. Since AC has the ability to partially dehydrate dissolved ions, this may lead to an increased Mg-incorporation into the Mg-Cc. To further quantify the adsorption of Ca^{2+} and Mg^{2+} on AC we suggest carrying out additional adsorption experiments with AC in further studies.

Furthermore, the formation conditions of the recently discovered CCHH phase in our present approach should be verified in a further study. Since CCHH is a thermodynamically metastable phase, its needle-shaped morphology could no longer be observed at the time of the SEM analysis (after one week of reaction time), since the CCHH had probably already transformed within this period.

However, a mineral phase with platelike morphology could be observed in subsamples of those experiments where originally CCHH could be detected by XRD, ATR-FTIR spectroscopy and in-situ Raman and which was subsequently transformed into the intermediate phase Mhc. In our study, an uncommon and significant Mg-incorporation into the final solids was detected, where mainly Arg with a very fast growing nanocrystalline structure occurred and in which partial Mg-substitution is suggested to occur at its structural defect positions. Further investigations by electron probe micro analysis (EPMA) of the precipitates could provide insights on the Mg-incorporation and elemental distribution of the resulting Arg. Since the observed platelike morphology of precipitates was only identified by SEM and could not be analyzed in more detail (Fig. 5 and Fig. 17), it can only be assumed that this phase represents $CaCO_3 \bullet ¾ H_2O$. Furthermore, in the present study it was not possible to determine exactly how much Mg^{2+} was incorporated into the CCHH structure. Further studies should therefore be focused on (i) the precise determination of the $CaCO_3 \bullet ¾ H_2O$ mineral phase and (ii) the incorporation of Mg^{2+} (with / without additions of AC e.g. to investigate the impact of its desolvation-effect) into the structure of CCHH and consequently its effect on the mineralogical evolution.

7. References

(1) Aizenberg J., Muller D. A., Grazul J. L. and Hamann D. R. **(2003)** Direct Fabrication of Large Micropatterned Single Crystals. Science, 299, 1205–1208.

(2) Aizenberg J., Weiner S. and Addadi L. **(2003)** Coexistence of Amorphous and Crystalline Calcium Carbonate in Skeletal Tissues. Connective Tissue Research, 44, 20–25.

(3) Andersen F. A. and Brečević L. **(1991)** Infrared spectra of amorphous and crystalline calcium carbonate. Acta Chemica Scandinavica 45, 1018–1024.

(4) Aufort J.; Demichelis R. **(2020)** Magnesium Impurities Decide the Structure of Calcium Carbonate Hemihydrate. Crystal Growth & Design. 20. 8028-8038.

(5) Bansal R. C.; Goyal M. **(2005)** Activated Carbon Adsorptions. CRC Press, Taylor & Francis. 1st Edition. 520.

(6) Bischoff W. D.; Sharma S. K.; MacKenzie F. T. **(1985)** American Mineralogist. Volume 70, Number 5-6. 581−589.

(7) Blue C. R.; Giuffre A.; Mergelsberg S.; Han N.; De Yoreo J. J.; Dove P. M. **(2017)** Chemical and Physical Controls on the Transformation of Amorphous Calcium Carbonate into Crystalline CaCO3 Polymorphs. Geochimica et Cosmochimica Acta 196, 179−196.

(8) Bots P.; Benning L. G.; Rodriguez-Blanco J.-D.; Roncal-Herrero T. and Shaw S. **(2012)** Mechanistic insights into the crystallization of amorphous calcium carbonate (ACC). Crystal Growth & Design 12, 3806–3814.

(9) Böttcher M. E.; Gehlken P.-L. and Steele D. F. **(1997)** Characterization of inorganic and biogenic magnesian calcites by Fourier Transform infrared spectroscopy. Solid State Ionics Volume 101–103, Part 2. 1379–1385.

(10) Brečević L. and Nielsen A. E. **(1989)** Solubility of Amorphous Calcium Carbonate. Journal of Crystal Growth 98 (3), 504−510.

(11) Brown T. L.; LeMay H. E.; Bursten B. E. **(2011)** Chemie - Studieren kompakt. Pearson 10. Auflage. 1011.

(12) Coleyshaw E. E.; Crump G. and Griffith W. P. **(2003)** Vibrational spectra of the hydrated carbonate minerals ikaite, monohydrocalcite, landsfordite and nesquehonite. Spectrochimica Acta Part A. Volume 59, Issue 10, 2231–2239.

(13) Dietzel M. **(2011)** Carbonates. In Encyclopedia of Geobiology (eds. J. Reitner and V. Thiel). Springer, Berlin, pp. 261–266.

(14) Devol R. T.; Sun C.; Marcus M. A.; Coppersmith S. N.; Myneni S. C. B.; Gilbert P. U. P. A. **(2015)** Nanoscale Transforming Mineral Phases in Fresh Nacre. J. Am. Chem. Soc. 2015, 137, 13325−13333.

(15) Edwards H. G. M.; Villar S. E. J.; Jehlicka J.; Munshi T. **(2005)** Spectrochimica Acta, Part A 61, 2273−2280.

(16)Fernández-Díaz L.; Putnis A.; Prieto M.; Putnis C.V. **(1996)** The role of magnesium the Crystallization of calcite and aragonite in a porous medium. Journal of sedimentary research, 66 (3) 482-491.

(17)Foran E.; Weiner S.; Fine M. **(2013)** Biogenic Fish-gut Calcium Carbonate is a Stable Amorphous Phase in the Gilt-head Seabream, Sparus aurata, Scientific Reports 1700.

(18)Gal A.; Habraken W.; Dvir G.; Fratzl P.; Weiner S.; Addadi L. **(2012)** Calcite Growth by a Solid-State Transformation of Stabilized Amorphous Calcium Carbonate Nanospheres in a Hydrogel. Angewandte Chemie International Edition. 52. 4867-4870.

(19)Geisler T.; Perdikouri C.; Kasioptas A. and Dietzel M. **(2012)** Real-time monitoring of the overall exchange of oxygen isotopes between aqueous CO_3^{2-} and H_2O by Raman spectroscopy. Geochimica et Cosmochimica Acta 90, 1–11.

(20)Giuffre A. J.; Gagnon A. C., Yoreo J. J.; Dove P. M. **(2015)** Isotopic tracer evidence for the amorphous calcium carbonate to calcite transformation by dissolution-reprecipitation. Geochimica et Cosmochimica Acta 165. 407-417.

(21)Goldsmith J. R.; Graf D. L. and Heard H. C. **(1961)** Lattice constants of the calcium magnesium carbonates. American Mineralogist. 46, 453–459.

(22)Griesshaber E.; Kelm K.; Sehrbrock A.; Mader W.; Mutterlose J.; Brand U.; Schmahl W. W. **(2009)** Amorphous calcium carbonate in the shell material of the brachiopod Megerlia truncate, European Journal of Minerlogy 21(4), 715−723.

(23)Habraken W.J.E.M.; Masic A.; Bertinetti L.; Al-Sawalmih A.; Glazer L.; Bentov S.; Fratzl P.; Sagi A.; Aichmayer B.; Berman A. **(2015)** Layered growth of crayfish gastrolith: About the stability of amorphous calcium carbonate and role of additives, Journal of Structural Biology 189 28–36.

(24)Han T. Y.-J. and Aizenberg J. **(2008)** Calcium Carbonate Storage in Amorphous Form and Its Template-Induced Crystallization. Chemistry of Materials 20, 1064–1068.

(25)Konrad F.; Gallien F.; Gerard D. E. and Dietzel M. **(2016)** Transformation of Amorphous Calcium Carbonate in Air, Crystal Growth & Design, 16(11), 6310–6317.

(26)Konrad F.; Purgstaller B.; Gallien F.; Mavromatis V.; Gane P.; Dietzel M. **(2018)** Influence of aqueous Mg concentration on the transformation of amorphous calcium carbonate, Journal of Crystal Growth. 498, 381-390.

(27)Kontoyannis C. G. and Vagenas V. **(2000)** Calcium carbonate phase analysis using XRD and FT-Raman spectroscopy. The Analyst 125(2), 251–255.

(28)Kralj D. and Brečević L. **(1995)** Dissolution kinetics and solubility of calcium carbonate monohydrate. Colloids and Surfaces A: Physicochemical and Engineering Aspects 96, 287-293.

(29)Loste E.; Wilson R. M.; Seshadri R. and Meldrum F. C. **(2003)** The role of magnesium in stabilising amorphous calcium carbonate and controlling calcite morphologies. Journal of Crystal Growth Volume 254, Issue 1. 206–218.

(30)Ma Y.; Aichmayer B.; Paris O.; Fratzl P.; Meibom A.; Metzler R. A.; Politi Y.; Addadi L.; Gilbert P. U. P. A.; Weiner S. **(2009)** The Grinding Tip of the Sea Urchin Tooth Exhibits Exquisite Control over Calcite Crystal Orientation and Mg Distribution. Proc. Natl. Acad. Sci. U. S. A., 106 (15), 6048−6053.

(31)Morse J. W. and Mackenzie F. T. **(1990)** Geochemistry of sedimentary carbonates. Dev. Sed. 48, 707.

(32)Mackenzie F. T.; Bischoff W. B.; Bishop F. C.; Loijens M.; Schoonmaker J.; Wollast R. **(1983)** Magnesian calcites: low temperature occurrence, solubility and solid-solution behavior. In Carbonates, Mineralogy and Chemistry (ed. R. J. Reeder). Book Crafters, Chelsea, Mich, 97–144.

(33)Marsh H.; Rodríguez-Reinoso F. **(2006)** Activated Carbon. Elsevier 1. 536.

(34)Németh P.; Mugnaioli E.; Gemmi M.; Czuppon G.; Demény A.; Spötl C. **(2018)** A nanocrystalline monoclinic $CaCO_3$ precursor of metastable aragonite. Science Advances 4(12). 1-6.

(35)Okrusch M.; Matthes S. **(2014)** Mineralogie – Eine Einführung in die spezielle Mineralogie, Petrologie und Lagerstättenkunde. Springer, 9.Auflage. 728.

(36)Polishchuk I.; Bracha A. A.; Bloch L.; Levy D.; Kozachkevich S.; Etinger-Geller Y.; Kauffmann Y.; Burghammer M.; Giacobbe C.; Villanova J. **(2017)** Coherently Aligned Nanoparticles within a Biogenic Single Crystal: A Biological Prestressing Strategy. Science. 358 (6368), 1294−1298.

(37)Politi Y.; Arad T.; Klein E.; Weiner S.; Addadi L. **(2004)** Sea Urchin spine calcite forms via a transient amorphous calcium carbonate phase. Science, 306 (5699), 1161−1164.

(38)Politi Y.; Batchelor D. R.; Zaslansky P.; Chmelka B. F.; Weaver J. C.; Sagi I.; Weiner S. and Addadi L. **(2010)** Role of Magnesium Ion in the Stabilization of Biogenic Amorphous Calcium Carbonate: A Structure-Function Investigation, Chemistry of Materials 22(1), 161–166.

(39)Prehal C.; Koczwara C., Jäckel N.; Schreiber A.; Burian M.; Amenitsch H.; Hartmann M. A.; Presser V.; Paris O. **(2017)** Quantification of ion confinement and desolvation in nanoporous carbon supercapacitors with modelling and in situ X-ray scattering. Nature energy 2, 16215.

(40)Press F.; Siever R.; Grotzinger J.; Jordan T.H. **(2008)** Allgemeine Geologie. Spektrum 5.Auflage 735.

(41)Purgstaller B.; Dietzel M.; Baldermann A.; Mavromatis V. **(2017)** Control of temperature and aqueous Mg^{2+}/Ca^{2+} ratio on the (trans-)formation of ikaite. Geochimica et Cosmochimica Acta, 217, 128-143.

(42)Purgstaller B.; Goetschl K. E.; Mavromatis V.; Dietzel M. **(2019)** Solubility investigations in the amorphous calcium magnesium carbonate system. Royal Society of Chemistry, CrystEngComm, 21, 155-164.

(43)Purgstaller B.; Konrad F.; Dietzel M.; Immenhauser A.; Mavromatis V. **(2017)** Control of Mg^{2+}/Ca^{2+} activity ratio on the formation of crystalline carbonate minerals via an amorphous precursor, Crystal Growth & Design 1069–1078.

(44)Purgstaller B.; Mavromatis V.; Immenhauser A.; Dietzel M. **(2016)** Transformation of Mg-Bearing Amorphous Calcium Carbonate to Mg-Calcite - In Situ Monitoring. Geochimica et Cosmochimica Acta, 174, 180−195.

(45)Radha A. V.; Forbes T. Z.; Killian C. E.; Gilbert P. U. P. A.; Navrotsky A. **(2010)** Transformation and crystallization energetics of synthetic and biogenic amorphous calcium carbonate. PNAS 107. 38, 16438-16443.

(46)Raz S.; Hamilton P. C.; Wilt F. H.; Weiner S. and Addadi L. **(2003)** Advanced Functional Materials, 13, 480–486.

(47)Raz S.; Testeniere O.; Hecker A.; Weiner S.; Luquet G. **(2002)** Stable Amorphous Calcium Carbonate Is the Main Component of the Calcium Storage Structures of the Crustacean Orchestia cavimana, Biol. Bull. 203, 269–274.

(48)Rostamian R.; Heidarpour M.; Mousavi S. F.; Afyuni M. **(2014)** Removal of Calcium and Magnesium by Activated Carbons Produced from Agricultural Wastes. Advances in Environmental Biology 8(12). 202-208.

(49)Ruiz-Henandez S. E.; Garu-Crespo R.; Almora-Barrios N.; Wolthers M.; Ruiz-Salvador A. R.; Fernandez N.; Leeuw N. H. **(2012)** Mg/Ca Partitioning Between Aqueous Solution and Aragonite Mineral: A Molecular Dynamics Study. Chemistry: A European Journal 18. 9828-9833.

(50)Ungár T. **(2004)** Microstructural parameters from X-ray diffraction peak broadening. Scripta Materialia 51, 777-781.

(51)Wang D.; Hamm L. M.; Bodnar R. J. and Dove P. M. **(2012)** Raman spectroscopic characterization of the magnesium content in amorphous calcium carbonates. Journal of Raman Spectroscopy. Volume 43, Issue 4. 543–548.

(52)Wang Z.; Hu P.; Gaetani G.; Liu C.; Saenger C.; Cohen A.; Hart S.; **(2013)** Experimental calibration of Mg isotope fractionation between aragonite and seawater. Geochimica et Cosmochimica Acta, 102. 113–123.

(53)Wang D. and Li Z. **(2012)** Chemical Modeling of Nesquehonite Solubility in $Li+Na+K+NH_4+Mg+Cl+H_2O$ System with a Speciation-based Approach, Chinese Journal of Chemical Engineering, 20. 267–276.

(54)Weiner S. and Dove P. M. **(2003)** An overview of biomineralization processes and the problem of the vital effect Dove, P. M., De Yoreo, J. J. and Weiner, S. (eds.). Biomineralization. Rev. Mineral. Geochem. 54, 1–29 and 249–283.

(55)Xto J. M.; Du H., Borca C. N., Amstad E., Bokhoven J. A., Huthwelker T. **(2019)** Tuning the Incorporation of Magnesium into Calcite during Its Crystallization from Additive-Free Aqueous Solution. Crystal Growth & Design. 1-10.

(56)Yao Q.; Wang Y.; Zhang Y.; Li H.; Zhou G. **(2019)** A biomimetic experimental study of magnesium ion mineralization in Mg-enriched aragonite. Science China Earth Science. 62. 1619-1629.

(57)Zou Z.; Wouter J. E. M.; Matveeva G.; Jensen A. C. S.; Bertinetti L.; Hood M. A.; Sun C.; Gilbert P. U. P. A.; Polishchuk I.; Pokroy B.; Mahamid J.; Politi Y.; Weiner S.; Werner P.; Bette S.; Dinnebier R.; Kolb U.; Zolotoyabko E.; Fratzl P. **(2019)** A Hydrated Crystalline Calcium Carbonate Phase: Calcium Carbonate Hemihydrate. Science, 363 (6425), 396−400.